

Vacancy-induced tunable Kondo effect in twisted bilayer graphene

Yueqing Chang,^{1,2,*} Jinjing Yi,^{1,2} Ang-Kun Wu,^{1,2} Fabian B. Kugler,^{3,1,2}
Eva Y. Andrei,¹ David Vanderbilt,^{1,2} Gabriel Kotliar,^{1,2,4} and J. H. Pixley^{1,2,3,†}

¹Department of Physics and Astronomy, Rutgers University, Piscataway, NJ 08854, USA

²Center for Materials Theory, Rutgers University, Piscataway, NJ 08854, USA

³Center for Computational Quantum Physics, Flatiron Institute, 162 5th Avenue, New York, NY 10010, USA

⁴Condensed Matter Physics and Materials Science Department, Brookhaven National Laboratory, Upton, NY 11973, USA

(Dated: October 7, 2024)

In single sheets of graphene, vacancy-induced states have been shown to host an effective spin-1/2 hole that can be Kondo-screened at low temperatures. Here, we show how these vacancy-induced impurity states survive in twisted bilayer graphene (TBG), which thus provides a tunable system to probe the critical destruction of the Kondo effect in pseudogap hosts. Ab-initio calculations and atomic-scale modeling are used to determine the nature of the vacancy states in the vicinity of the magic angle in TBG, demonstrating that the vacancy can be treated as a quantum impurity. Utilizing this insight, we construct an Anderson impurity model with a TBG host that we solve using the numerical renormalization group combined with the kernel polynomial method. We determine the phase diagram of the model and show how there is a strict dichotomy between vacancies in the AA/BB versus AB/BA tunneling regions. In AB/BA vacancies, the Kondo temperature at the magic angle develops a broad distribution with a tail to vanishing temperatures due to multifractal wavefunctions at the magic angle. We argue that scanning tunneling microscopy in the vicinity of the vacancy can act as a probe of both the critical single-particle states and the underlying many-body ground state in magic-angle TBG.

Twisted van der Waals heterostructures have taken the condensed matter community by storm [1–4]. Since the first experimental evidence of the band reconstruction and emergence of a flat band in twisted bilayer graphene (TBG) at twist angle $\sim 1^\circ$ [5], a wide range of experimental and technical breakthroughs [6–9] have paved the way for the discovery and reproducible observations of correlated insulating states [10] and superconductivity [11] in magic-angle TBG, highlighting the vast potential and intriguing properties of these moiré materials [12–37]. These ideas have now been extended to twisted bilayer transition metal dichalcogenides (TMD) [38–42], quantum magnets [43, 44], high-temperature superconductors [45–49], and bosonic superfluids in optical lattices [50–53]. To unravel the nature of the underlying many-body states in moiré materials, it is essential to explore new ways to extract electron correlations while using current experimental capabilities.

One potentially fruitful direction is to probe the nature of impurity states, accurately measurable with scanning tunneling microscopy (STM), to gain insights into the many-body ground state that the impurity states are coupled to. For instance, tunneling spectra of impurity-induced resonances in superconductors reveal signatures of the pairing symmetry [54]. For single sheets of graphene, creating impurity states strongly coupled to the itinerant electrons was a challenge until it was realized that vacancy-induced bound states act like a spin-1/2 hole, originating from the vacancy's nearest-neighbor σ states which couple to the π -band due to the local curvature near the vacancy site [55–60]. This represents a clear-cut realization of the pseudogap Anderson impurity model (AIM), which features a quantum critical point at non-zero Kondo coupling [61–73]. Yet, experimentally observing this quantum critical point has remained out of reach due to the lack of tunability of vacancy states, despite the ob-

ervation of Kondo screening in graphene hosts [59, 74].

In this work, we study vacancy-induced impurity states in TBG away from and at the magic angle with atomic-scale and effective lattice models. Using ab-initio calculations, we show that a vacancy [75] induces an effective spin-1/2 hole on the atomic scale and compute the hybridization between the vacancy and the twisted pair of π -bands, showing a clear dichotomy between AA/BB and AB/BA regions. This is in stark contrast to the recent description of TBG as a topological Kondo lattice problem with suitably defined “impurity” limits (i.e., realizing local moments on the moiré scale) [30–37, 76]. Here, we focus on atomic-scale vacancies that arise in realistic experimental settings across a wide array of moiré materials (e.g., graphene [77], TMD [78, 79], cuprate superconductors [80, 81]). We use ab-initio derived vacancy states to construct an effective quantum impurity model for a realistic vacancy, which is solved by combining the kernel polynomial method [82] and the numerical renormalization group [83] (KPM+NRG [84]). Away from the magic angle, this realizes a tunable, pseudogap AIM where twisting the bilayers tunes the vacancy through its quantum phase transition. At the magic angle, the impurity is always Kondo-screened at low temperatures. We study the distribution of Kondo temperatures T_K across the sample to show how T_K in the AB region is strongly suppressed relative to the AA region.

Microscopic picture.—To set the stage, we investigate how the vacancy σ (V_σ) state in TBG at the magic angle ($\theta_M = 1.05^\circ$ [85]) hybridizes with the twisted pair of π -bands using an accurate machine-learned tight-binding model [86], combined with embedded V_σ states from density functional theory (DFT) calculations [87]. Figure 1(c) shows the structure of TBG at θ_M obtained by fully relaxing free-standing TBG using the interatomic potential model [110–112] with the method described in Ref. [113, 114], using the molecu-

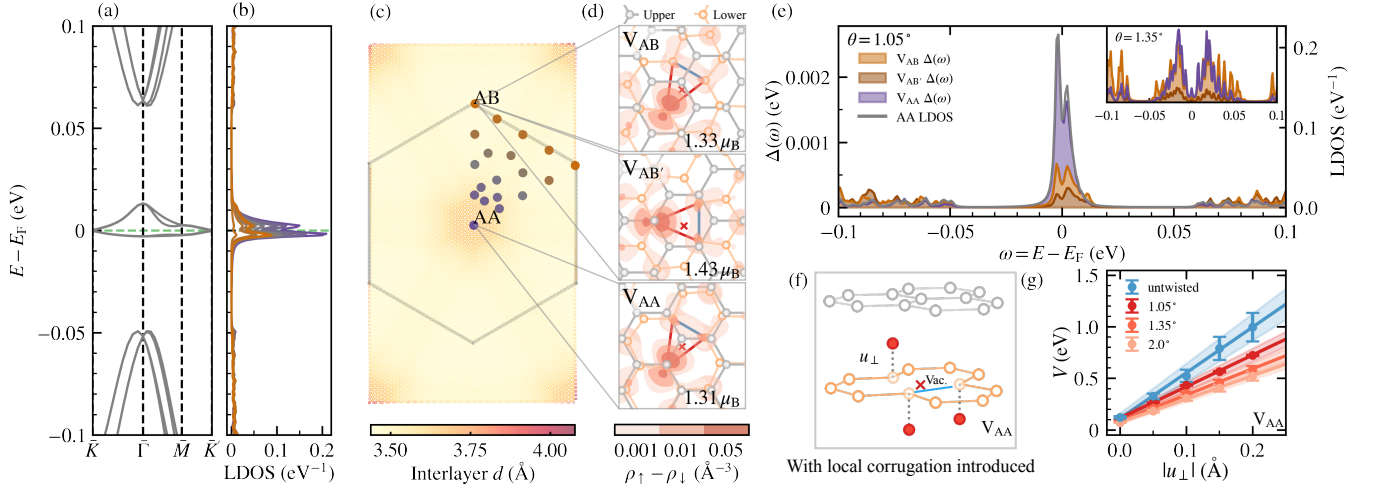


FIG. 1. Atomic-scale modeling of TBG with a vacancy. (a) Band structure of pristine TBG at θ_M without vacancy. \bar{K} and \bar{K}' indicate the two valleys of the moiré Brillouin zone. (b) Projected local density of states (LDOS) at the potential vacancy sites denoted in (c), color-coded. (c) The C atoms in the relaxed pristine TBG at θ_M , with the center of AA and AB regions annotated. The atoms are colored-coded according to the local interlayer spacing. The hexagon represents the moiré unit cell. The 19 potential vacancy sites chosen for computing the LDOS in (b) are indicated by thicker dots. (d) $\rho_\uparrow - \rho_\downarrow$ for three typical vacancy configurations, computed in untwisted bilayer graphene using DFT. V_{AB} and $V_{AB'}$ vacancies could be present in TBG AB regions, while V_{AA} vacancies are typical in AA regions. The grey (orange) circles denote the C atoms in the upper (lower) layers, and the red cross denotes the vacancy. The blue (red) lines highlight the shorter (longer) distances between three adjacent sites. The clouds of $\rho_\uparrow - \rho_\downarrow$ are plotted in red, showing that most of the excessive spin is contributed by the σ -lobe at the isolated adjacent site. (e) Hybridization function at θ_M between the V_σ state and the TBG bath for the three vacancy configurations. The LDOS for the AA site is also plotted in the grey curve for comparison. The insets show the hybridization at $\theta = 1.35^\circ$, which features a Dirac-cone-like low-energy dispersion with larger flat-band bandwidth compared to 1.05° . (f) Side view of AA-stacked bilayer graphene near the vacancy site, with manual vertical displacements of the three adjacent sites away from equilibrium, denoted by u_\perp . The bonded sites (connected by a blue line) are displaced downward by the same u_\perp . (g) Hybridization strength V between the V_σ state and the bath versus u_\perp for the untwisted V_{AA} vacancy (blue) and when coupled to the TBG bath (red). Lines are linear fits, showing that V is tunable by u_\perp and θ .

lar dynamics (MD) simulation package LAMMPS [115]. The in-plane and out-of-plane atomic relaxations manifest in enlarged AB/BA regions, consistent with previous work [113, 114, 116–119]. Figure 1(a) shows the band structure of fully relaxed pristine TBG in the atomic-scale tight-binding model, and Fig. 1(b) the local density of states (LDOS) projected onto the potential vacancy sites indicated in panel (c). The flat-band states are mostly localized in the AA regions (except at Γ) and have decreasing projections onto sites further away from the AA center. This indicates that an impurity in the AA (AB) regions hybridizes more (less) with the localized flat-band states.

To understand microscopically how vacancy states hybridize with the π -bands in TBG, we first consider a monovacancy in single-layer graphene. Removing one atom leaves dangling vacancy V_π and V_σ orbitals at the three adjacent atoms, which undergo a Jahn–Teller distortion so that one isolated atom moves further away from the vacancy, and the other two atoms move closer to re-bond. This leads to one V_σ state localized at the isolated site near the Fermi level and a V_π quasi-localized zero mode [56, 57]. In the experimentally relevant regime, the effect of the V_π zero mode can be qualitatively captured by a renormalization of the V_σ Coulomb interaction [59]; we thus focus on the V_σ state in the following.

In single-layer graphene, the coupling between the V_σ state and the π -bands requires finite local corrugation that breaks the mirror symmetry [59, 60]. This coupling arises natu-

rally if a second, untwisted layer is stacked onto free-standing graphene, which breaks the mirror symmetry near the vacancy site in the lower layer. To capture this, we performed DFT calculations using a 6×6 supercell of free-standing untwisted bilayer graphene with one vacancy in the bottom layer in three typical local environments [87], named after the registry of the two sheets of graphene. Note that, in AB-stacked graphene, there are two types of vacancies, V_{AB} and $V_{AB'}$ (see Fig. 1(d)). Similar to single-layer graphene, the three adjacent atoms near the vacancy site relax to a final equilibrium configuration with almost no corrugation near the vacancy. Figure 1(d) shows the calculated excessive spin density, $\rho_\uparrow - \rho_\downarrow$ [120], which is centered at the isolated adjacent C atom, contributed mainly by the σ -lobe toward the vacancy. The details of the calculations and the electronic structure of bilayer graphene with a vacancy are summarized in [87].

In the dilute limit, we expect the 6×6 supercell simulation of the V_σ state in untwisted bilayer graphene to mimic the actual vacancy in TBG near θ_M . Using our DFT results in untwisted bilayer graphene, we compute the hybridization function between the dangling V_σ state and the “bath” (TBG *without* the vacancy and its three adjacent sites) from the microscopic model, $\Delta_{\text{micro}}(\omega) = \pi \sum_{n,\mathbf{k}} |V_{n\mathbf{k}}|^2 \delta(\omega - \epsilon_{n\mathbf{k}})$. Here, $V_{n\mathbf{k}} = \langle \phi_{V_\sigma} | H_{V_\sigma\text{-bath}} \mathcal{P}_{\text{bath-TBG}} | \psi_{n\mathbf{k}} \rangle$ represents the tunneling matrix element between the V_σ state $|\phi_{V_\sigma}\rangle$ and the pristine TBG eigenstate $|\psi_{n\mathbf{k}}\rangle$ with eigenvalue $\epsilon_{n\mathbf{k}}$. $H_{V_\sigma\text{-bath}}$ is the hopping between the V_σ state and the C atoms in the bath;

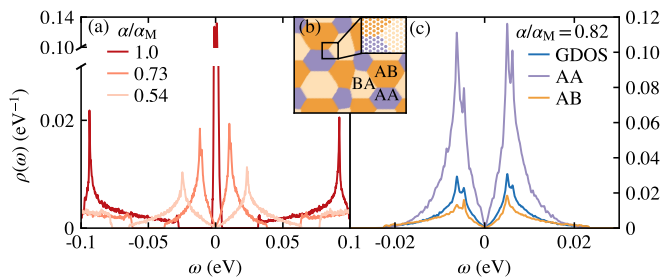


FIG. 2. **Hybridization functions for the effective lattice model of TBG** in Eq. (1). (a) The model GDOS at different twist parameters, where $\alpha = 0.081$ ($w = 0.11$ eV) corresponds to the magic angle. (b) Tunneling map, where different colors indicate the locally dominating tunneling according to the effective lattice model [87]. The inset shows the microscopic lattice spacing across a patch. (c) Comparison of GDOS and LDOS in the AA and AB regions at $\alpha = 0.067$ ($w = 0.09$ eV). The LDOS is averaged over 200 samples of random twisted boundary conditions; the GDOS is additionally averaged over the origin of rotation in TBG across 400 samples.

$\mathcal{P}_{\text{bath-TBG}}$ projects the TBG eigenstate from the Hilbert space of N -site TBG to that of the $(N-1)$ -orbital π bath. Figure 1(e) shows $\Delta_{\text{micro}}(\omega)$ for the three vacancy environments at θ_M and the LDOS at the AA center, with insets showing the result at 1.35° . In comparison, V_{AA} hybridizes much stronger with the bath, especially with the flat-band states.

In experiments, the substrate almost always induces local corrugation in TBG, which is not captured in our MD simulations. Therefore, we manually introduced local corrugation near the vacancy to study how it changes the hybridization. Figure 1(f) shows a schematic side view of how the three vacancy-adjacent atoms are displaced by u_\perp either upward or downward [87] for a V_{AA} vacancy. Figure 1(g) shows that the hybridization strength V increases with u_\perp and decreases with θ . For $u_\perp > 0.2$ Å, a localized V_σ state can no longer be identified. We find that V_{AA} vacancies are more sensitive to twisting [87].

In summary, a vacancy in bilayer graphene induces a localized spin density, which hybridizes with the π -bath with a strength tunable via the local environment, atomic corrugation, and the twist angle, suggesting that TBG with a monovacancy realizes a tunable, pseudogap AIM. To make the AIM tractable, we construct an effective model with the impurity parameters derived from the microscopic model and the hybridization function from a simpler TBG bath. The latter has all of the salient features we have just found and allows us to describe the spectral properties of TBG down to sufficiently low energy scales to treat the Kondo effect accurately.

Quantum impurity model.—We use the AIM, with the Hamiltonian $H = H_{\text{host}} + H_{\text{hyb}} + H_{\text{imp}}$, to emulate TBG with a vacancy. The host contributions are typically written in the single-particle eigenbasis, where ϵ_k is the eigenenergy of a state created by $c_{k\sigma}^\dagger$ with a wavefunction $\phi_{k\sigma}(j) = \langle j, \sigma | \epsilon_k \rangle$ at lattice site j [121]. Then,

$$H_{\text{host}} = \sum_{k,\sigma} \epsilon_k c_{k\sigma}^\dagger c_{k\sigma}, \quad H_{\text{hyb}} = V \sum_{\sigma} (d_{\sigma}^\dagger c_{R\sigma} + \text{H.c.}), \quad (1)$$

where R labels the impurity site, $c_{R\sigma} = \sum_k \phi_k(R) c_{k\sigma}$, and $V > 0$ is the hybridization strength. The effect of the host on the impurity is described by the hybridization function

$$\Delta_R(\omega) = \pi V^2 \sum_k |\phi_k(R)|^2 \delta(\omega - \epsilon_k) \equiv \pi V^2 \rho_R(\omega), \quad (2)$$

with ρ_R the host LDOS per spin orientation ($\phi_k \equiv \phi_{k\sigma}$). One approximation we consider to help gain physical insight into the problem ignores the spatial contribution of the wavefunction to the LDOS, so that the LDOS in the hybridization function is replaced by the global DOS (GDOS, per spin orientation, per lattice site) $\rho(\omega) = N^{-1} \sum_k \delta(\omega - \epsilon_k)$.

To describe the ω -dependence of $\Delta_R(\omega)$, we use a microscopic lattice model of TBG [122] derived from the Bistritzer–MacDonald (BM) continuum model [85, 87], which can be scaled up in system size, provides higher resolution for the ultra-low-energy features in the LDOS and captures the emergent multifractality in TBG’s wavefunctions at θ_M [87]. We can modify $\Delta_R(\omega)$ by varying either the twist angle θ or the interlayer tunneling w , since only their ratio matters at small twist angles in the form $\alpha \equiv w/[2v_F k_D \sin(\theta/2)]$. Here, the Fermi velocity is $v_F = 3ta_0/(2\hbar)$ with $t = 2.8$ eV, and the distance from the Γ to the Dirac point is $k_D = 4\pi/(3a_0)$ with $a_0 \approx 2.46$ Å the graphene lattice constant. It is more convenient for us to vary w at fixed $\theta = 1.05^\circ$ as we treat the incommensurate twist via a rational approximation. The magic angle α_M then occurs at $w = 0.11$ eV.

We focus on the charge neutrality point and show the DOS of the TBG lattice model in Fig. 2(a). Relaxation in the lattice model is accounted for by breaking the symmetry in the tunneling between the AA and AB regions, with $w_{AA}/w_{AB} = 0.75$ [123]. In the BM model, the GDOS can have a charge neutrality van Hove singularity at the magic angle, which (ignoring how the impurity is embedded in the host) leads to Kondo screening of the impurity [76]. Incorporating the impurity location, the tunneling strengths in the lattice model mark different sublattice tunneling geometries dominated by AA/BB or AB/BA regions (Fig. 2(b)). The LDOS in each representative region, depicted in Fig. 2(c) away from α_M , reflects how the probability density of wavefunctions in the miniband are concentrated near the AA sites, consistent with our atomic-scale model results [87] and expectations from previous TBG Wannier-function calculations [14, 15, 124–126].

Finally, the impurity part in the Hamiltonian reads

$$H_{\text{imp}} = \epsilon_d (\hat{n}_{d\uparrow} + \hat{n}_{d\downarrow}) + U \hat{n}_{d\uparrow} \hat{n}_{d\downarrow}. \quad (3)$$

An impurity state with spin σ and on-site repulsion U , localized at the vacancy site R , is created by d_{σ}^\dagger , has a number operator $\hat{n}_{d\sigma} = d_{\sigma}^\dagger d_{\sigma}$, and an energy ϵ_d measured from the host Fermi energy $E_F = 0$. We choose $U = 2.2$ eV and $\epsilon_d = -0.5$ eV as motivated by our microscopic analysis [87]. Note that the hybridization functions already break particle-hole symmetry and that the TBG half bandwidth (of the full

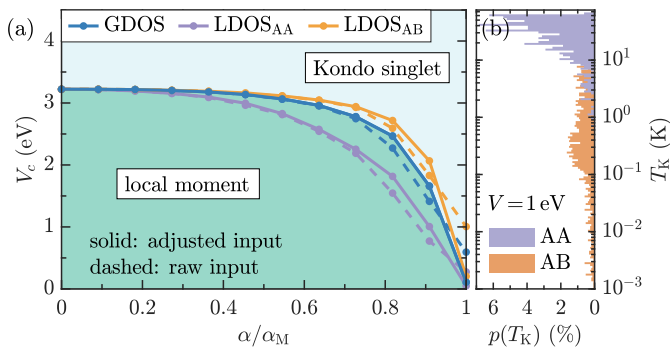


FIG. 3. **Solution of the quantum impurity model.** (a) Phase diagram at $T = 0$. The critical hybridization strength V_c that separates the local-moment ($\mu_{\text{eff}} = 1/4$) and Kondo-singlet phase ($\mu_{\text{eff}} = 0$) as a function of $\alpha = w/[2v_F k_D \sin(\theta/2)]$ vanishes linearly at the magic angle $\alpha_M \approx 1/\sqrt{3}$ (cf. Eq. (4)). Dashed lines show results for $\Delta \propto \rho$ with the GDOS ρ or with an LDOS ρ_R (R in the AA or AB region), see Eq. (2). For the solid lines, the input is adjusted to match the analytically known asymptotic low-energy behavior [87]. (b) Distribution of T_K for different impurity locations across magic-angle TBG. We consider $V = 1$ eV and roughly 500 (1500) sites for the AA (AB) region. The AB, compared to the AA distribution, is broader, centered at a smaller value, and has a tail reaching down to very low T_K .

spectrum, not only the miniband) D depends weakly on α , $D(\alpha) \approx 8$ eV. Below, the hybridization strength is either varied or chosen as $V = 1$ eV to estimate the typical T_K . The effective Kondo coupling is $J \sim V^2/U$.

Many-body solution.—We first consider the $T = 0$ phase diagram for a vacancy in TBG with variable hybridization strength V and twist parameter α . A single sheet of graphene realizes a clear-cut pseudogap AIM with a local-moment and Kondo-singlet phase. Away from α_M , the GDOS of TBG still follows the pseudogap behavior: at low energies, $\rho(\omega) \sim |\omega|/v^2$, where $v = v(\alpha)$ is the renormalized Dirac velocity. As $v(\alpha)$ vanishes at α_M ($\alpha_M \approx 1/\sqrt{3}$ for the first magic angle in [85]), we may expand it as $v(\alpha) \sim |\alpha - \alpha_M|$ close to α_M . From previous NRG studies, we know that such a particle-hole asymmetric pseudogap AIM has a critical Kondo coupling J_c with $\rho_0 J_c \sim \mathcal{O}(1)$ [63–65, 70, 127]. Hence, from $\rho_0 \sim 1/v^2(\alpha)$, we expect

$$J_c \sim |\alpha - \alpha_M|^2 \Leftrightarrow V_c \sim |\alpha - \alpha_M|. \quad (4)$$

At α_M , $\rho(\omega)$ is smooth at low ω with finite $\rho(0)$. Hence, at $T = 0$, a Kondo-singlet phase is found for arbitrarily small V .

We use KPM with a linear lattice size $L = 569a_0$ [122] and an expansion order of $N_C = 2^{18}$ to calculate the Wilson-chain coefficients. Then, from the NRG impurity contribution to the spin susceptibility χ_{imp} , we extract the effective magnetic moment $\mu_{\text{eff}} = \lim_{T \rightarrow 0} T \chi_{\text{imp}}(T)$. This yields a phase diagram, Fig. 3(a), where the local-moment and Kondo-singlet phases are characterized by $\mu_{\text{eff}} = 1/4$ and $\mu_{\text{eff}} = 0$, respectively. $V_c(\alpha)$ for hybridization functions proportional to an LDOS (with R in either the AA or AB region) and to the GDOS (equivalent to the R -averaged LDOS) behave qualita-

tively similarly. As expected, in the AA region, the enhanced LDOS leads to a smaller V_c relative to the AB/BA regions. For the GDOS, we can use the asymptotic low-energy behavior mentioned before ($\rho(\omega)|_{\alpha \neq \alpha_M} \sim |\omega|$, $\rho(\omega)|_{\alpha_M} = \text{const}$) to adjust and extend the Wilson-chain input at energy scales below the KPM resolution [87]. The data with adjusted input nicely reproduces Eq. (4) and confirms our expectations: There is a finite V_c for all $\alpha \neq \alpha_M$, decreasing linearly with α close to α_M . At $\alpha = \alpha_M$, any $V > 0$ leads to Kondo screening, consistent with a recent study using the GDOS in TBG [76].

Focusing on α_M , where the ground state is always Kondo-screened, we may ask below which T the Kondo-singlet phase occurs across the sample, i.e., how T_K changes with the location of the impurity at fixed V (say, 1 eV). We use $T_K \simeq 1/|4\chi_{\text{loc}}|$ [128] as a robust and efficient estimate, where $\chi_{\text{loc}} = \partial_h \langle S^z \rangle|_{h=0}$ (with $\langle S^z \rangle$ the local magnetization) is the local susceptibility computed at $T = 0$. In Fig. 3(b), we plot the distribution of Kondo scales found for a large number of different sites. There is a strict dichotomy between vacancies in the AA versus AB regions. The LDOS throughout the AA region is rather similar, leading to a narrow distribution of Kondo scales. By contrast, the LDOS in the AB region varies widely at low energies (as it includes V_{AB} and $V_{AB'}$ contributions) and is generally smaller than in the AA region. This leads to a broad distribution of Kondo scales, centered at a smaller value than in the AA region, and with a tail to vanishing T_K . This tail is a signature of a broad distribution we expect [84, 129–131] to result from the multifractal wavefunctions at the magic angle that arise in several incommensurate models of TBG [51, 132] including H_{host} in Eq. (1) (see [87]).

In reality, the TBG bath becomes correlated very close to θ_M , and the non-interacting bath description breaks down. Therefore, at $T = 0$, our results are directly applicable across the majority of the phase diagram in Fig. 3(a), while future work is needed to incorporate the strongly correlated bath that can induce a gap at charge neutrality [133]. At finite temperatures above the correlated gap, our results serve as a description of the normal state of the defect-induced Kondo effect in TBG.

Conclusion.—Using ab-initio calculations, we embedded a vacancy into pristine TBG and demonstrated how it hybridizes with the low-energy miniband in the vicinity of the magic angle. From this insight, we built an effective AIM that we solved with KPM+NRG [84]. We found a variety of many-body ground states and a pseudogap quantum critical point tunable by the twist angle. At the magic angle, the vacancy is always Kondo-screened, leading to a distribution of Kondo temperatures that is broad in the AB region due to the underlying multifractal single-particle eigenstates [51, 132]. We propose the STM response of such Kondo-induced vacancy states as a probe of the underlying many-body ground states in TBG and moiré materials more broadly.

Acknowledgments.—We thank Kevin Ingersent and Justin Wilson for insightful discussions and collaborations on related work. Y.C. thanks Tawfiqur Rakib for help in setting up MD simulations for TBG, and Shang Ren and Michele Pizzochero

for valuable discussions. This work has been supported in part by the NSF CAREER Grant No. DMR 1941569 (A.K.W., J.H.P.), the BSF Grant No. 2020264 (J.Y., J.H.P.), the Alfred P. Sloan Foundation through a Sloan Research Fellowship (J.H.P.), Department of Energy DOE-FG02-99ER45742 (E.Y.A.), the Gordon and Betty Moore Foundation EPiQS initiative GBMF9453 (E.Y.A.), the NSF Grant No. DMR 1954856 (D.V.), and the U.S. Department of Energy, Office of Science, Office of Advanced Scientific Computing Research, and Office of Basic Energy Sciences, Scientific Discovery through Advanced Computing (SciDAC) program (G.K.). F.B.K. acknowledges support by the Alexander von Humboldt Foundation through the Feodor Lynen Fellowship. Y.C. acknowledges support from the Abrahams Postdoctoral Fellowship of the Center for Materials Theory at Rutgers University. The KPM computations were performed using the Beowulf cluster at the Department of Physics and Astronomy of Rutgers University and the Amarel cluster provided by the Office of Advanced Research Computing (OARC) [134] at Rutgers, The State University of New Jersey. The NRG results were obtained using the QSpace tensor library developed by A. Weichselbaum [135] and the NRG toolbox by Seung-Sup B. Lee [136–138]. The Flatiron Institute is a division of the Simons Foundation.

* yueqing.chang@rutgers.edu

† jed.pixley@physics.rutgers.edu

- [1] E. Y. Andrei and A. H. MacDonald, Graphene bilayers with a twist, *Nat. Mater.* **19**, 1265 (2020).
- [2] L. Balents, C. R. Dean, D. K. Efetov, and A. F. Young, Superconductivity and strong correlations in moiré flat bands, *Nat. Phys.* **16**, 725 (2020).
- [3] E. Y. Andrei, D. K. Efetov, P. Jarillo-Herrero, A. H. MacDonald, K. F. Mak, T. Senthil, E. Tutuc, A. Yazdani, and A. F. Young, The marvels of moiré materials, *Nat. Rev. Mater.* **6**, 201 (2021).
- [4] K. P. Nuckolls and A. Yazdani, A microscopic perspective on moiré materials, *Nat. Rev. Mater.* [10.1038/s41578-024-00682-1](https://doi.org/10.1038/s41578-024-00682-1) (2024).
- [5] G. Li, A. Luican, J. M. B. Lopes Dos Santos, A. H. Castro Neto, A. Reina, J. Kong, and E. Y. Andrei, Observation of Van Hove singularities in twisted graphene layers, *Nat. Phys.* **6**, 109 (2010).
- [6] A. Luican, G. Li, A. Reina, J. Kong, R. R. Nair, K. S. Novoselov, A. K. Geim, and E. Y. Andrei, Single-Layer Behavior and Its Breakdown in Twisted Graphene Layers, *Phys. Rev. Lett.* **106**, 126802 (2011).
- [7] W. Yan, M. Liu, R.-F. Dou, L. Meng, L. Feng, Z.-D. Chu, Y. Zhang, Z. Liu, J.-C. Nie, and L. He, Angle-Dependent van Hove Singularities in a Slightly Twisted Graphene Bilayer, *Phys. Rev. Lett.* **109**, 126801 (2012).
- [8] K. Kim, M. Yankowitz, B. Fallahazad, S. Kang, H. C. P. Movva, S. Huang, S. Larentis, C. M. Corbet, T. Taniguchi, K. Watanabe, S. K. Banerjee, B. J. LeRoy, and E. Tutuc, van der Waals Heterostructures with High Accuracy Rotational Alignment, *Nano Lett.* **16**, 1989 (2016).
- [9] Y. Cao, J. Luo, V. Fatemi, S. Fang, J. Sanchez-Yamagishi, K. Watanabe, T. Taniguchi, E. Kaxiras, and P. Jarillo-Herrero, Superlattice-Induced Insulating States and Valley-Protected Orbits in Twisted Bilayer Graphene, *Phys. Rev. Lett.* **117**, 116804 (2016).
- [10] Y. Cao, V. Fatemi, A. Demir, S. Fang, S. L. Tomarken, J. Y. Luo, J. D. Sanchez-Yamagishi, K. Watanabe, T. Taniguchi, E. Kaxiras, R. C. Ashoori, and P. Jarillo-Herrero, Correlated insulator behaviour at half-filling in magic-angle graphene superlattices, *Nature* **556**, 80 (2018).
- [11] Y. Cao, V. Fatemi, S. Fang, K. Watanabe, T. Taniguchi, E. Kaxiras, and P. Jarillo-Herrero, Unconventional superconductivity in magic-angle graphene superlattices, *Nature* **556**, 43 (2018).
- [12] D. K. Efimkin and A. H. MacDonald, Helical network model for twisted bilayer graphene, *Phys. Rev. B* **98**, 035404 (2018).
- [13] C. Xu and L. Balents, Topological Superconductivity in Twisted Multilayer Graphene, *Phys. Rev. Lett.* **121**, 087001 (2018).
- [14] J. Kang and O. Vafek, Symmetry, Maximally Localized Wannier States, and a Low-Energy Model for Twisted Bilayer Graphene Narrow Bands, *Phys. Rev. X* **8**, 031088 (2018).
- [15] M. Koshino, N. F. Q. Yuan, T. Koretsune, M. Ochi, K. Kuroki, and L. Fu, Maximally Localized Wannier Orbitals and the Extended Hubbard Model for Twisted Bilayer Graphene, *Phys. Rev. X* **8**, 031087 (2018).
- [16] B. Padhi, C. Setty, and P. W. Phillips, Doped Twisted Bilayer Graphene near Magic Angles: Proximity to Wigner Crystallization, Not Mott Insulation, *Nano Lett.* **18**, 6175 (2018).
- [17] F. Guinea and N. R. Walet, Electrostatic effects, band distortions, and superconductivity in twisted graphene bilayers, *Proc. Natl. Acad. Sci. U.S.A.* **115**, 13174 (2018).
- [18] G. Tarnopolsky, A. J. Kruchkov, and A. Vishwanath, Origin of Magic Angles in Twisted Bilayer Graphene, *Phys. Rev. Lett.* **122**, 106405 (2019).
- [19] J. Liu, J. Liu, and X. Dai, Pseudo Landau level representation of twisted bilayer graphene: Band topology and implications on the correlated insulating phase, *Phys. Rev. B* **99**, 155415 (2019).
- [20] J. Kang and O. Vafek, Strong Coupling Phases of Partially Filled Twisted Bilayer Graphene Narrow Bands, *Phys. Rev. Lett.* **122**, 246401 (2019).
- [21] M. Xie and A. H. MacDonald, Nature of the Correlated Insulator States in Twisted Bilayer Graphene, *Phys. Rev. Lett.* **124**, 097601 (2020).
- [22] N. Bultinck, E. Khalaf, S. Liu, S. Chatterjee, A. Vishwanath, and M. P. Zaletel, Ground State and Hidden Symmetry of Magic-Angle Graphene at Even Integer Filling, *Phys. Rev. X* **10**, 031034 (2020).
- [23] O. Vafek and J. Kang, Renormalization Group Study of Hidden Symmetry in Twisted Bilayer Graphene with Coulomb Interactions, *Phys. Rev. Lett.* **125**, 257602 (2020).
- [24] B. A. Bernevig, Z.-D. Song, N. Regnault, and B. Lian, Twisted bilayer graphene. I. Matrix elements, approximations, perturbation theory, and a $k \cdot p$ two-band model, *Phys. Rev. B* **103**, 205411 (2021).
- [25] Z.-D. Song, B. Lian, N. Regnault, and B. A. Bernevig, Twisted bilayer graphene. II. Stable symmetry anomaly, *Phys. Rev. B* **103**, 205412 (2021).
- [26] B. A. Bernevig, Z.-D. Song, N. Regnault, and B. Lian, Twisted bilayer graphene. III. Interacting Hamiltonian and exact symmetries, *Phys. Rev. B* **103**, 205413 (2021).
- [27] B. Lian, Z.-D. Song, N. Regnault, D. K. Efetov, A. Yazdani, and B. A. Bernevig, Twisted bilayer graphene. IV. Exact insulator ground states and phase diagram, *Phys. Rev. B* **103**,

- 205414 (2021).
- [28] B. A. Bernevig, B. Lian, A. Cowsik, F. Xie, N. Regnault, and Z.-D. Song, Twisted bilayer graphene. V. Exact analytic many-body excitations in Coulomb Hamiltonians: Charge gap, Goldstone modes, and absence of Cooper pairing, *Phys. Rev. B* **103**, 205415 (2021).
- [29] O. Vafek and J. Kang, Lattice model for the Coulomb interacting chiral limit of magic-angle twisted bilayer graphene: Symmetries, obstructions, and excitations, *Phys. Rev. B* **104**, 075143 (2021).
- [30] Z.-D. Song and B. A. Bernevig, Magic-Angle Twisted Bilayer Graphene as a Topological Heavy Fermion Problem, *Phys. Rev. Lett.* **129**, 047601 (2022).
- [31] H. Hu, B. A. Bernevig, and A. M. Tsvelik, Kondo Lattice Model of Magic-Angle Twisted-Bilayer Graphene: Hund's Rule, Local-Moment Fluctuations, and Low-Energy Effective Theory, *Phys. Rev. Lett.* **131**, 026502 (2023).
- [32] Y.-Z. Chou and S. Das Sarma, Kondo Lattice Model in Magic-Angle Twisted Bilayer Graphene, *Phys. Rev. Lett.* **131**, 026501 (2023).
- [33] D. Călugăru, M. Borovkov, L. L. H. Lau, P. Coleman, Z.-D. Song, and B. A. Bernevig, Twisted Bilayer Graphene as Topological Heavy Fermion: II. Analytical approximations of the model parameters, *Low Temp. Phys.* **49**, 640 (2023).
- [34] L. L. H. Lau and P. Coleman, *Topological Mixed Valence Model for Twisted Bilayer Graphene* (2023), arXiv:2303.02670.
- [35] G.-D. Zhou, Y.-J. Wang, N. Tong, and Z.-D. Song, Kondo phase in twisted bilayer graphene, *Phys. Rev. B* **109**, 045419 (2024).
- [36] Y.-Z. Chou and S. Das Sarma, Scaling theory of intrinsic Kondo and Hund's rule interactions in magic-angle twisted bilayer graphene, *Phys. Rev. B* **108**, 125106 (2023).
- [37] H. Hu, G. Rai, L. Crippa, J. Herzog-Arbeitman, D. Călugăru, T. Wehling, G. Sangiovanni, R. Valentí, A. M. Tsvelik, and B. A. Bernevig, Symmetric Kondo Lattice States in Doped Strained Twisted Bilayer Graphene, *Phys. Rev. Lett.* **131**, 166501 (2023).
- [38] F. Wu, T. Lovorn, E. Tutuc, and A. H. MacDonald, Hubbard Model Physics in Transition Metal Dichalcogenide Moiré Bands, *Phys. Rev. Lett.* **121**, 026402 (2018).
- [39] E. C. Regan, D. Wang, C. Jin, M. I. Bakti Utama, B. Gao, X. Wei, S. Zhao, W. Zhao, Z. Zhang, K. Yumigeta, M. Blei, J. D. Carlström, K. Watanabe, T. Taniguchi, S. Tongay, M. Crommie, A. Zettl, and F. Wang, Mott and generalized Wigner crystal states in WSe_2/WS_2 moiré superlattices, *Nature* **579**, 359 (2020).
- [40] Z. Zhang, Y. Wang, K. Watanabe, T. Taniguchi, K. Ueno, E. Tutuc, and B. J. LeRoy, Flat bands in twisted bilayer transition metal dichalcogenides, *Nat. Phys.* **16**, 1093 (2020).
- [41] L. Wang, E.-M. Shih, A. Ghiotto, L. Xian, D. A. Rhodes, C. Tan, M. Claassen, D. M. Kennes, Y. Bai, B. Kim, K. Watanabe, T. Taniguchi, X. Zhu, J. Hone, A. Rubio, A. N. Pasupathy, and C. R. Dean, Correlated electronic phases in twisted bilayer transition metal dichalcogenides, *Nat. Mat.* **19**, 861 (2020).
- [42] A. Ghiotto, E.-M. Shih, G. S. S. G. Pereira, D. A. Rhodes, B. Kim, J. Zang, A. J. Millis, K. Watanabe, T. Taniguchi, J. C. Hone, L. Wang, C. R. Dean, and A. N. Pasupathy, Quantum criticality in twisted transition metal dichalcogenides, *Nature* **597**, 345 (2021).
- [43] Q. Tong, F. Liu, J. Xiao, and W. Yao, Skyrmions in the Moiré of van der Waals 2D Magnets, *Nano Lett.* **18**, 7194 (2018).
- [44] K. Hejazi, Z.-X. Luo, and L. Balents, Noncollinear phases in moiré magnets, *Proc. Natl. Acad. Sci. U.S.A.* **117**, 10721 (2020).
- [45] O. Can, T. Tummuru, R. P. Day, I. Elfimov, A. Damascelli, and M. Franz, High-temperature topological superconductivity in twisted double-layer copper oxides, *Nat. Phys.* **17**, 519 (2021).
- [46] Y. Zhu, M. Liao, Q. Zhang, H.-Y. Xie, F. Meng, Y. Liu, Z. Bai, S. Ji, J. Zhang, K. Jiang, R. Zhong, J. Schneeloch, G. Gu, L. Gu, X. Ma, D. Zhang, and Q.-K. Xue, Presence of s -Wave Pairing in Josephson Junctions Made of Twisted Ultrathin $Bi_2Sr_2CaCu_2O_{8+x}$ Flakes, *Phys. Rev. X* **11**, 031011 (2021).
- [47] P. A. Volkov, J. H. Wilson, K. P. Lucht, and J. H. Pixley, Magic angles and correlations in twisted nodal superconductors, *Phys. Rev. B* **107**, 174506 (2023).
- [48] P. A. Volkov, J. H. Wilson, K. P. Lucht, and J. Pixley, Current and Field-Induced Topology in Twisted Nodal Superconductors, *Phys. Rev. Lett.* **130**, 186001 (2023).
- [49] S. Y. F. Zhao, X. Cui, P. A. Volkov, H. Yoo, S. Lee, J. A. Gardener, A. J. Akey, R. Engelke, Y. Ronen, R. Zhong, G. Gu, S. Plugge, T. Tummuru, M. Kim, M. Franz, J. H. Pixley, N. Poccia, and P. Kim, Time-reversal symmetry breaking superconductivity between twisted cuprate superconductors, *Science* **382**, 1422 (2023).
- [50] A. González-Tudela and J. I. Cirac, Cold atoms in twisted-bilayer optical potentials, *Phys. Rev. A* **100**, 053604 (2019).
- [51] Y. Fu, E. J. König, J. H. Wilson, Y.-Z. Chou, and J. H. Pixley, Magic-angle semimetals, *npj Quantum Mater.* **5**, 71 (2020).
- [52] X.-W. Luo and C. Zhang, Spin-Twisted Optical Lattices: Tunable Flat Bands and Larkin-Ovchinnikov Superfluids, *Phys. Rev. Lett.* **126**, 103201 (2021).
- [53] Z. Meng, L. Wang, W. Han, F. Liu, K. Wen, C. Gao, P. Wang, C. Chin, and J. Zhang, Atomic Bose-Einstein condensate in twisted-bilayer optical lattices, *Nature* **615**, 231 (2023).
- [54] P. O. Sukhachov, F. von Oppen, and L. I. Glazman, Tunneling spectra of impurity states in unconventional superconductors, *Phys. Rev. B* **108**, 024505 (2023).
- [55] P. Haase, S. Fuchs, T. Pruschke, H. Ochoa, and F. Guinea, Magnetic moments and Kondo effect near vacancies and resonant scatterers in graphene, *Phys. Rev. B* **83**, 241408 (2011).
- [56] J. J. Palacios and F. Ynduráin, Critical analysis of vacancy-induced magnetism in monolayer and bilayer graphene, *Phys. Rev. B* **85**, 245443 (2012).
- [57] B. R. K. Nanda, M. Sherafati, Z. S. Popović, and S. Satpathy, Electronic structure of the substitutional vacancy in graphene: density-functional and Green's function studies, *New J. Phys.* **14**, 083004 (2012).
- [58] J. Mao, Y. Jiang, D. Moldovan, G. Li, K. Watanabe, T. Taniguchi, M. R. Masir, F. M. Peeters, and E. Y. Andrei, Realization of a tunable artificial atom at a supercritically charged vacancy in graphene, *Nat. Phys.* **12**, 545 (2016).
- [59] Y. Jiang, P.-W. Lo, D. May, G. Li, G.-Y. Guo, F. B. Anders, T. Taniguchi, K. Watanabe, J. Mao, and E. Y. Andrei, Inducing Kondo screening of vacancy magnetic moments in graphene with gating and local curvature, *Nat. Commun.* **9**, 2349 (2018).
- [60] D. May, P.-W. Lo, K. Deltenre, A. Henke, J. Mao, Y. Jiang, G. Li, E. Y. Andrei, G.-Y. Guo, and F. B. Anders, Modeling of the gate-controlled Kondo effect at carbon point defects in graphene, *Phys. Rev. B* **97**, 155419 (2018).
- [61] D. Withoff and E. Fradkin, Phase transitions in gapless Fermi systems with magnetic impurities, *Phys. Rev. Lett.* **64**, 1835 (1990).
- [62] R. Bulla, T. Pruschke, and A. C. Hewson, Anderson impurity in pseudo-gap Fermi systems, *J. Phys.: Condens. Matter* **9**, 10463 (1997).
- [63] C. Gonzalez-Buxton and K. Ingersent, Renormalization-group

- study of Anderson and Kondo impurities in gapless Fermi systems, *Phys. Rev. B* **57**, 14254 (1998).
- [64] K. Ingersent and Q. Si, Critical Local-Moment Fluctuations, Anomalous Exponents, and ω/t Scaling in the Kondo Problem with a Pseudogap, *Phys. Rev. Lett.* **89**, 076403 (2002).
- [65] L. Fritz and M. Vojta, Phase transitions in the pseudogap Anderson and Kondo models: Critical dimensions, renormalization group, and local-moment criticality, *Phys. Rev. B* **70**, 214427 (2004).
- [66] M. Vojta and L. Fritz, Upper critical dimension in a quantum impurity model: Critical theory of the asymmetric pseudogap Kondo problem, *Phys. Rev. B* **70**, 094502 (2004).
- [67] L. Fritz, S. Florens, and M. Vojta, Universal crossovers and critical dynamics of quantum phase transitions: A renormalization group study of the pseudogap Kondo problem, *Phys. Rev. B* **74**, 144410 (2006).
- [68] M. T. Glossop, S. Kirchner, J. H. Pixley, and Q. Si, Critical Kondo Destruction in a Pseudogap Anderson Model: Scaling and Relaxational Dynamics, *Phys. Rev. Lett.* **107**, 076404 (2011).
- [69] J. H. Pixley, S. Kirchner, K. Ingersent, and Q. Si, Quantum criticality in the pseudogap Bose-Fermi Anderson and Kondo models: Interplay between fermion- and boson-induced Kondo destruction, *Phys. Rev. B* **88**, 245111 (2013).
- [70] L. Fritz and M. Vojta, The physics of Kondo impurities in graphene, *Rep. Prog. Phys.* **76**, 032501 (2013).
- [71] J. H. Pixley, T. Chowdhury, M. T. Miecznikowski, J. Stephens, C. Wagner, and K. Ingersent, Entanglement entropy near Kondo-destruction quantum critical points, *Phys. Rev. B* **91**, 245122 (2015).
- [72] C. Wagner, T. Chowdhury, J. Pixley, and K. Ingersent, Long-Range Entanglement near a Kondo-Destruction Quantum Critical Point, *Phys. Rev. Lett.* **121**, 147602 (2018).
- [73] A. Cai, J. H. Pixley, K. Ingersent, and Q. Si, Critical local moment fluctuations and enhanced pairing correlations in a cluster Anderson model, *Phys. Rev. B* **101**, 014452 (2020).
- [74] J.-H. Chen, L. Li, W. G. Cullen, E. D. Williams, and M. S. Fuhrer, Tunable Kondo effect in graphene with defects, *Nat. Phys.* **7**, 535 (2011).
- [75] T. O. Wehling, A. M. Black-Schaffer, and A. V. Balatsky, Dirac materials, *Adv. Phys.* **63**, 1 (2014).
- [76] A. S. Shankar, D. O. Oriekhov, A. K. Mitchell, and L. Fritz, Kondo effect in twisted bilayer graphene, *Phys. Rev. B* **107**, 245102 (2023).
- [77] F. Dietrich, U. J. Guevara, A. Tiutiunnyk, D. Laroze, and E. Cisternas, Vacancies and Stone–Wales defects in twisted bilayer graphene – A comparative theoretical study, *FlatChem* **41**, 100541 (2023).
- [78] S. Wang, A. Robertson, and J. H. Warner, Atomic structure of defects and dopants in 2D layered transition metal dichalcogenides, *Chem. Soc. Rev.* **47**, 6764 (2018).
- [79] H. Guo, X. Zhang, and G. Lu, Moiré excitons in defective van der Waals heterostructures, *Proc. Natl. Acad. Sci. U.S.A.* **118**, e2105468118 (2021).
- [80] S. H. Pan, E. W. Hudson, K. M. Lang, H. Eisaki, S. Uchida, and J. C. Davis, Imaging the effects of individual zinc impurity atoms on superconductivity in $\text{Bi}_2\text{Sr}_2\text{CaCu}_2\text{O}_{8+\delta}$, *Nature* **403**, 746 (2000).
- [81] H. Alloul, J. Bobroff, M. Gabay, and P. J. Hirschfeld, Defects in correlated metals and superconductors, *Rev. Mod. Phys.* **81**, 45 (2009).
- [82] A. Weiße, G. Wellein, A. Alvermann, and H. Fehske, The kernel polynomial method, *Rev. Mod. Phys.* **78**, 275 (2006).
- [83] R. Bulla, T. A. Costi, and T. Pruschke, Numerical renormalization group method for quantum impurity systems, *Rev. Mod. Phys.* **80**, 395 (2008).
- [84] A.-K. Wu, D. Bauernfeind, X. Cao, S. Gopalakrishnan, K. Ingersent, and J. H. Pixley, Aubry-André Anderson model: Magnetic impurities coupled to a fractal spectrum, *Phys. Rev. B* **106**, 165123 (2022).
- [85] R. Bistritzer and A. H. MacDonald, Moiré bands in twisted double-layer graphene, *Proc. Natl. Acad. Sci. U.S.A.* **108**, 12233 (2011).
- [86] S. Pathak, T. Rakib, R. Hou, A. Nevidomskyy, E. Ertekin, H. T. Johnson, and L. K. Wagner, Accurate tight-binding model for twisted bilayer graphene describes topological flat bands without geometric relaxation, *Phys. Rev. B* **105**, 115141 (2022).
- [87] See Supplemental Material at [url], which includes Refs. [88–109], for additional information about the details of atomic-scale simulations, construction of the impurity model, discussions about emergent multifractality, and further details of numerical renormalization group calculations.
- [88] G. Kresse and J. Hafner, *Ab initio* molecular dynamics for liquid metals, *Phys. Rev. B* **47**, 558 (1993).
- [89] G. Kresse and J. Furthmüller, Efficiency of ab-initio total energy calculations for metals and semiconductors using a plane-wave basis set, *Comput. Mater. Sci.* **6**, 15 (1996).
- [90] G. Kresse and J. Furthmüller, Efficient iterative schemes for *ab initio* total-energy calculations using a plane-wave basis set, *Phys. Rev. B* **54**, 11169 (1996).
- [91] J. P. Perdew, K. Burke, and M. Ernzerhof, Generalized Gradient Approximation Made Simple, *Phys. Rev. Lett.* **77**, 3865 (1996).
- [92] P. A. Thrower and R. M. Mayer, Point defects and self-diffusion in graphite, *Physica Status Solidi (a)* **47**, 11 (1978).
- [93] M. Leccese and R. Martinazzo, Anomalous delocalization of resonant states in graphene & the vacancy magnetic moment, *Electron. Struct.* **5**, 024010 (2023).
- [94] V. G. Miranda, L. G. G. V. Dias Da Silva, and C. H. Lewenkopf, Coulomb charging energy of vacancy-induced states in graphene, *Phys. Rev. B* **94**, 075114 (2016).
- [95] M. Schüler, M. Rösner, T. O. Wehling, A. I. Lichtenstein, and M. I. Katsnelson, Optimal Hubbard Models for Materials with Nonlocal Coulomb Interactions: Graphene, Silicene, and Benzene, *Phys. Rev. Lett.* **111**, 036601 (2013).
- [96] H. J. Changlani, H. Zheng, and L. K. Wagner, Density-matrix based determination of low-energy model Hamiltonians from ab initio wavefunctions, *J. Chem. Phys.* **143**, 102814 (2015).
- [97] N. Marzari and D. Vanderbilt, Maximally localized generalized Wannier functions for composite energy bands, *Phys. Rev. B* **56**, 12847 (1997).
- [98] A. A. Mostofi, J. R. Yates, Y.-S. Lee, I. Souza, D. Vanderbilt, and N. Marzari, wannier90: A tool for obtaining maximally-localised Wannier functions, *Comput. Phys. Commun.* **178**, 685 (2008).
- [99] A. A. Mostofi, J. R. Yates, G. Pizzi, Y.-S. Lee, I. Souza, D. Vanderbilt, and N. Marzari, An updated version of wannier90: A tool for obtaining maximally-localised Wannier functions, *Comput. Phys. Commun.* **185**, 2309 (2014).
- [100] G. Pizzi, V. Vitale, R. Arita, S. Blügel, F. Freimuth, G. Géranton, M. Gibertini, D. Gresch, C. Johnson, T. Koretsune, J. Ibañez-Azpiroz, H. Lee, J.-M. Lihm, D. Marchand, A. Marrazzo, Y. Mokrousov, J. I. Mustafa, Y. Nohara, Y. Nomura, L. Paulatto, S. Poncé, T. Ponweiser, J. Qiao, F. Thöle, S. S. Tsirkin, M. Wierzbowska, N. Marzari, D. Vanderbilt, I. Souza, A. A. Mostofi, and J. R. Yates, Wannier90 as a community code: new features and applications, *J. Phys.: Con-*

- dens. Matter* **32**, 165902 (2020).
- [101] V. Dobrosavljević, T. R. Kirkpatrick, and B. G. Kotliar, Kondo effect in disordered systems, *Phys. Rev. Lett.* **69**, 1113 (1992).
- [102] E. Miranda, V. Dobrosavljević, and G. Kotliar, Kondo disorder: a possible route towards non-Fermi-liquid behaviour, *J. Phys.: Condens. Matter* **8**, 9871 (1996).
- [103] P. S. Cornaglia, D. R. Grempel, and C. A. Balseiro, Universal Distribution of Kondo Temperatures in Dirty Metals, *Phys. Rev. Lett.* **96**, 117209 (2006).
- [104] S. Kettemann, E. R. Mucciolo, and I. Varga, Critical Metal Phase at the Anderson Metal-Insulator Transition with Kondo Impurities, *Phys. Rev. Lett.* **103**, 126401 (2009).
- [105] V. G. Miranda, L. G. G. V. Dias da Silva, and C. H. Lewenkopf, Disorder-mediated Kondo effect in graphene, *Phys. Rev. B* **90**, 201101 (2014).
- [106] E. C. Andrade, A. Jagannathan, E. Miranda, M. Vojta, and V. Dobrosavljević, Non-fermi-liquid behavior in metallic quasicrystals with local magnetic moments, *Phys. Rev. Lett.* **115**, 036403 (2015).
- [107] A. M. Coe, G. Li, and E. Y. Andrei, Cryogen-free modular scanning tunneling microscope operating at 4-K in high magnetic field on a compact ultra-high vacuum platform, (2024), [arXiv:2404.05002 \[cond-mat.mes-hall\]](https://arxiv.org/abs/2404.05002).
- [108] R. Peters, T. Pruschke, and F. B. Anders, Numerical renormalization group approach to green's functions for quantum impurity models, *Phys. Rev. B* **74**, 245114 (2006).
- [109] A. Weichselbaum and J. von Delft, Sum-rule conserving spectral functions from the numerical renormalization group, *Phys. Rev. Lett.* **99**, 076402 (2007).
- [110] D. W. Brenner, O. A. Shenderova, J. A. Harrison, S. J. Stuart, B. Ni, and S. B. Sinnott, A second-generation reactive empirical bond order (REBO) potential energy expression for hydrocarbons, *Journal of Physics: Condensed Matter* **14**, 783 (2002).
- [111] A. N. Kolmogorov and V. H. Crespi, Registry-dependent interlayer potential for graphitic systems, *Phys. Rev. B* **71**, 235415 (2005).
- [112] W. Ouyang, D. Mandelli, M. Urbakh, and O. Hod, Nanoserpents: Graphene Nanoribbon Motion on Two-Dimensional Hexagonal Materials, *Nano Lett.* **18**, 6009 (2018), publisher: American Chemical Society.
- [113] T. Rakib, P. Pochet, E. Ertekin, and H. T. Johnson, Corrugation-driven symmetry breaking in magic-angle twisted bilayer graphene, *Commun. Phys.* **5**, 242 (2022).
- [114] K. Krongchon, T. Rakib, S. Pathak, E. Ertekin, H. T. Johnson, and L. K. Wagner, Registry-dependent potential energy and lattice corrugation of twisted bilayer graphene from quantum Monte Carlo, *Phys. Rev. B* **108**, 235403 (2023).
- [115] A. P. Thompson, H. M. Aktulga, R. Berger, D. S. Bolintineanu, W. M. Brown, P. S. Crozier, P. J. in 't Veld, A. Kohlmeyer, S. G. Moore, T. D. Nguyen, R. Shan, M. J. Stevens, J. Tranchida, C. Trott, and S. J. Plimpton, LAMMPS - a flexible simulation tool for particle-based materials modeling at the atomic, meso, and continuum scales, *Comp. Phys. Comm.* **271**, 108171 (2022).
- [116] S. Dai, Y. Xiang, and D. J. Srolovitz, Twisted Bilayer Graphene: Moiré with a Twist, *Nano Lett.* **16**, 5923 (2016).
- [117] K. Zhang and E. B. Tadmor, Structural and electron diffraction scaling of twisted graphene bilayers, *J. Mech. Phys. Solids* **112**, 225 (2018).
- [118] P. Lucignano, D. Alfè, V. Cataudella, D. Ninno, and G. Cantale, Crucial role of atomic corrugation on the flat bands and energy gaps of twisted bilayer graphene at the magic angle $\theta \sim 1.08^\circ$, *Phys. Rev. B* **99**, 195419 (2019).
- [119] H. Yoo, R. Engelke, S. Carr, S. Fang, K. Zhang, P. Cazeaux, S. H. Sung, R. Hovden, A. W. Tsen, T. Taniguchi, K. Watanabe, G.-C. Yi, M. Kim, M. Luskin, E. B. Tadmor, E. Kaxiras, and P. Kim, Atomic and electronic reconstruction at the van der Waals interface in twisted bilayer graphene, *Nat. Mater.* **18**, 448 (2019).
- [120] The spin \uparrow or \downarrow , given by a spin-polarized calculation, do not correspond to any real-space direction.
- [121] Here, k labels the eigenstate, but does not represent the momentum. The lattice model is defined on an incommensurate lattice. Therefore, momentum is not a well-defined quantum number.
- [122] J. H. Wilson, Y. Fu, S. Das Sarma, and J. H. Pixley, Disorder in twisted bilayer graphene, *Phys. Rev. Res.* **2**, 023325 (2020).
- [123] S. Carr, S. Fang, Z. Zhu, and E. Kaxiras, Exact continuum model for low-energy electronic states of twisted bilayer graphene, *Phys. Rev. Res.* **1**, 013001 (2019).
- [124] H. C. Po, L. Zou, T. Senthil, and A. Vishwanath, Faithful tight-binding models and fragile topology of magic-angle bilayer graphene, *Phys. Rev. B* **99**, 195455 (2019).
- [125] S. Carr, S. Fang, H. C. Po, A. Vishwanath, and E. Kaxiras, Derivation of Wannier orbitals and minimal-basis tight-binding Hamiltonians for twisted bilayer graphene: First-principles approach, *Phys. Rev. Res.* **1**, 033072 (2019).
- [126] S. Carr, S. Fang, and E. Kaxiras, Electronic-structure methods for twisted moiré layers, *Nat. Rev. Mater.* **5**, 748 (2020).
- [127] K. Chen and C. Jayaprakash, The Kondo effect in pseudo-gap Fermi systems: a renormalization group study, *J. Phys.: Condens. Matter* **7**, L491 (1995).
- [128] M. Filippone, C. P. Moca, A. Weichselbaum, J. von Delft, and C. Mora, At which magnetic field, exactly, does the Kondo resonance begin to split? A Fermi liquid description of the low-energy properties of the Anderson model, *Phys. Rev. B* **98**, 075404 (2018).
- [129] S. Kettemann, E. R. Mucciolo, I. Varga, and K. Slevin, Kondo-Anderson transitions, *Phys. Rev. B* **85**, 115112 (2012).
- [130] R. Gammag and K.-S. Kim, Distribution of critical temperature at Anderson localization, *Phys. Rev. B* **93**, 205128 (2016).
- [131] K. Slevin, S. Kettemann, and T. Ohtsuki, Multifractality and the distribution of the Kondo temperature at the Anderson transition, *EPJ B* **92**, 281 (2019), [arXiv:1910.00917 \[cond-mat\]](https://arxiv.org/abs/1910.00917).
- [132] M. Gonçalves, H. Z. Olyaei, B. Amorim, R. Mondaini, P. Ribeiro, and E. V. Castro, Incommensurability-induced sub-ballistic narrow-band-states in twisted bilayer graphene, *2D Mater.* **9**, 011001 (2021).
- [133] X. Lu, P. Stepanov, W. Yang, M. Xie, M. A. Aamir, I. Das, C. Urgell, K. Watanabe, T. Taniguchi, G. Zhang, A. Bachtold, A. H. MacDonald, and D. K. Efetov, Superconductors, orbital magnets and correlated states in magic-angle bilayer graphene, *Nature* **574**, 653 (2019).
- [134] [Http://oarc.rutgers.edu](http://oarc.rutgers.edu).
- [135] A. Weichselbaum, Non-abelian symmetries in tensor networks: A quantum symmetry space approach, *Ann. Phys.* **327**, 2972 (2012); Tensor networks and the numerical renormalization group, *Phys. Rev. B* **86**, 245124 (2012); X-symbols for non-abelian symmetries in tensor networks, *Phys. Rev. Res.* **2**, 023385 (2020).
- [136] S.-S. B. Lee and A. Weichselbaum, Adaptive broadening to improve spectral resolution in the numerical renormalization group, *Phys. Rev. B* **94**, 235127 (2016).
- [137] S.-S. B. Lee, J. von Delft, and A. Weichselbaum, Doublon-Holon Origin of the Subpeaks at the Hubbard Band Edges, *Phys. Rev. Lett.* **119**, 236402 (2017).

[138] S.-S. B. Lee, F. B. Kugler, and J. von Delft, Computing local multipoint correlators using the numerical renormalization

group, [Phys. Rev. X **11**, 041007 \(2021\)](#)

.

Supplementary information of “Vacancy induced tunable Kondo effect in twisted bilayer graphene”

Yueqing Chang,^{1,2} Jinjing Yi,^{1,2} Ang-Kun Wu,^{1,2} Fabian B. Kugler,^{3,1,2}
Eva Andrei,¹ David Vanderbilt,^{1,2} Gabriel Kotliar,^{1,2,4} and J. H. Pixley^{1,2,3}

¹*Department of Physics and Astronomy, Rutgers University, Piscataway, NJ 08854, USA*

²*Center for Materials Theory, Rutgers University, Piscataway, NJ 08854, USA*

³*Center for Computational Quantum Physics, Flatiron Institute, 162 5th Avenue, New York, NY 10010, USA*

⁴*Condensed Matter Physics and Materials Science Department, Brookhaven National Laboratory, Upton, NY 11973, USA*

CONTENTS

I. Ab-initio study of monovacancy in twisted bilayer graphene	1
A. DFT simulation of the monovacancy in untwisted bilayer graphene	1
B. Local corrugation enhances the V_σ -bath hybridization	4
C. General framework of the multi-scale modeling of dilute impurities in moiré heterostructures	6
D. Local corrugation away from equilibrium	7
E. Comparison between the microscopic model and the lattice model	8
II. Lattice model of TBG	9
III. Kernel polynomial method	9
A. Wavefunction from the lattice model of TBG	10
IV. Numerical renormalization group	12
References	12

I. AB-INITIO STUDY OF MONOVACANCY IN TWISTED BILAYER GRAPHENE

A. DFT simulation of the monovacancy in untwisted bilayer graphene

To study how local atomic environments affect the vacancy resonant states and take into account the V_σ states localized at the nearest neighbor sites, which occur near the Fermi level, we performed density functional theory (DFT) calculation of bilayer graphene with two different registries and three different vacancy configurations: V_{AA} , V_{AB} , $V_{AB'}$. For each bilayer structure, we constructed a 143-atom 6×6 supercell with a single vacancy at the bottom layer. The lattice relaxation and self-consistent-field calculations were performed using the Vienna Ab initio Simulation Package [S1–S3], with a fully spin-polarized Perdew-Burke-Ernzerhof exchange-correlation functional [S4] with a $6 \times 6 \times 1$ k -grid, with a force convergence tolerance $0.05 \text{ eV}/\text{\AA}$. The fully relaxed structures of the three different vacancy configurations exhibit a similar Jahn-Teller distortion near the vacancy, as shown in Fig. S1. The distortions show that one nearest-neighbor carbon atom moves away from the vacancy site, while the other two atoms move closer toward each other to re-bond. The equilibrium bond lengths l_1 , l_1 and l_2 satisfy $l_1 > l_0$ and $l_2 < l_0$, where l_0 is the equilibrium next-nearest-neighbor distance in the pristine single layer graphene.

We also noticed that the relaxation of $V_{AB'}$ takes a particularly long time since the potential energy surface of this type of vacancy is rougher and requires more time to resolve the lowest energy configuration. We plotted the two configurations that are very close in energy for $V_{AB'}$ in Fig. S2. We noticed that one can converge to the correct equilibrium configuration only with a finer k -grid (such as $6 \times 6 \times 1$) and a tighter force convergence tolerance. For the triangle formed by the three nearest-neighbor sites in $V_{AB'}$, there is no carbon site at the top, while for the V_{AA} or V_{AB} , the carbon site at the top of the triangle repels the lone σ and π electrons. Therefore, for $V_{AB'}$, another possible low-energy configuration (Fig. S2 right panel) is when two atoms come further, and one atom moves closer to the vacancy, leaving the total spin moment to be localized around two adjacent sites. While for V_{AA} and V_{AB} , repelled by the center-top carbon, two nearest-neighbor carbon sites always move closer to reform a 2-carbon bound state, significantly lowers the total energy and leads to faster convergence.

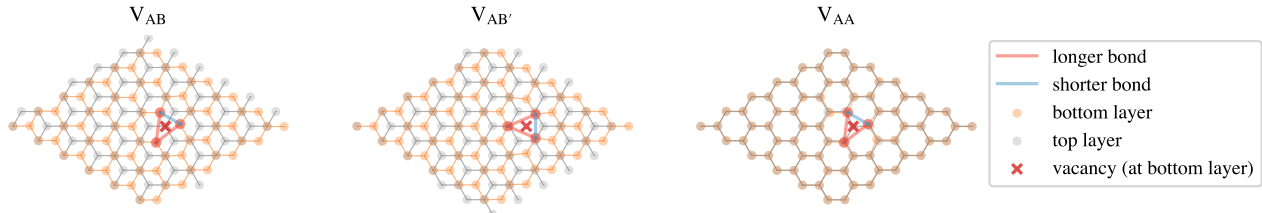


FIG. S1. Relaxed lattice structure of the 6×6 supercell of the bilayer graphene with vacancy systems in three different local environments, named after stacking registry. The vacancy is placed on the bottom layer, denoted by the red cross. The distorted isosceles triangle formed by the three nearest neighbors of the vacancy is denoted by red dots, with the red and blue lines annotating the longer and shorter bonds among them.

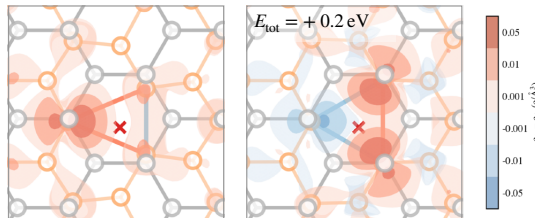


FIG. S2. The two $V_{AB'}$ distortions that are close in energies. The spin density $\rho_{\uparrow} - \rho_{\downarrow}$ isosurfaces are plotted for each configuration. We found that one can converge to the correct equilibrium configuration only with a finer k -grid (such as $6 \times 6 \times 1$) and a tighter force convergence tolerance.

We then performed fully spin-polarized self-consistent-field (SCF) calculations on these four structures using a uniform $3 \times 3 \times 1$ Monkhorst-Pack k -grid. The formation energies of these three types of vacancies, computed as $E(N-1) - \frac{N-1}{N}E(N)$ are listed in Table SI, comparable with the 7.0 ± 0.5 eV formation energy of a monovacancy in single-layer graphene as experimentally measured [S5]. For all three types of vacancies, the spin density $\rho_{\uparrow} - \rho_{\downarrow}$ localizes mainly on the further-away carbon, contributed mostly by the lone σ -electron, and partially by the lone π -electrons. The V_{σ} state and the zero-mode V_{π} state are occupied in the spin-up channel and empty in the spin-down channel, both contributing to the $S = 1$ ground state spin density localized around the three nearest-neighbor sites. Because of screening between the V_{π} state and the π bath, the V_{π} state's contribution to the final spin magnetic moment is about $0.4 \mu_B$, resulting in a total spin magnetic moment $\sim 1.4 \mu_B$ (Table SI). In comparison, the spin magnetic moment of the monovacancy in single-layer graphene ranges from 1.04 to $1.84 \mu_B$ [S6]. However, we point out that this discrepancy in μ_{tot} is likely due to a non-converged vertical displacement, sparse k -grid, and small supercell (high defect concentration) [S7]. Our calculation using a $12 \times 12 \times 1$ k -grid yielded 1.23 , 1.36 , and $1.21 \mu_B$ for the three vacancy types listed, slightly smaller than the values given by $6 \times 6 \times 1$ grid listed in Table SI. Also, note that the dispersion in the V_{σ} state might be greatly overestimated due to the vacancy-vacancy interaction introduced by the periodic boundary condition we used in DFT calculations. This might lead to an underestimated vacancy magnetic moment [S8], which should have a value that is closer to $2 \mu_B$ than $\sim 1.4 \mu_B$.

In addition, one can estimate the intra-band interaction U for the V_{σ} state. Assuming that the Hubbard model of an isolated impurity applies, the single-particle energies, ~ -0.5 and 1.8 eV, of the V_{σ} (occupied, spin up) and lowest unoccupied spin down V_{σ} states would be ϵ and $\epsilon + U$, i.e., the energies needed for the removing one electron, $|\sigma\rangle \rightarrow |0\rangle$ ($\sigma = \uparrow, \downarrow$) and adding one electron, $|\sigma\rangle \rightarrow |\uparrow\downarrow\rangle$. Here, $|0\rangle$, $|\sigma\rangle$, $|\uparrow\downarrow\rangle$ are the eigenstates of the isolated one-band impurity model, with on-site energy ϵ and Hubbard repulsion U . This allows us to estimate the value of intra-orbital Hubbard interaction U , which is listed in Table SI, in rough agreement with the value of 2.0 eV given by Ref. [S9]. The value is smaller than the intra-orbital onsite Hubbard repulsion computed to be 4.4 eV using the state-of-the-art constrained random phase approximations based on DFT results [S10], and 3.6 eV given by fixed-node diffusion Monte Carlo [S11] for carbon's p_z orbitals.

To study the hybridization of the vacancy states with the itinerant bands, we disentangled the Kohn-Sham wavefunctions near the Fermi level within a ~ 20 eV window and downfolded to a set of maximally-localized Wannier functions (MLWFs) [S12] using the Wannier90 package [S13–S15]. The initial guess of the projections includes atomic p_z orbitals on each carbon site and three sp^2 orbitals, with their lobes directed towards the vacancy site on the

	V_{AB}	$V_{AB'}$	V_{AA}
Formation energy (eV)	5.66	5.64	5.48
Total spin magnetic moment (μ_B), $k: 6 \times 6 \times 1$	1.33	1.43	1.31
(contribution of V_σ and V_π (μ_B))	1.0 0.33	1.0 0.43	1.0 0.31
V_σ on-site energy ϵ (eV)	-0.45	-0.48	-0.51
V_σ on-site Hubbard U (eV)	2.26	2.21	2.24
V_σ - π bath hybridization strength V (eV)	0.24(3)	0.13(1)	0.12(1)
(contribution from top layer V (eV))	0.12(1)	0.09(1)	0.07(1)

TABLE SI. Computed properties of the three vacancy configurations in equilibrium, along with the estimated intra-orbital Hubbard U and on-site energy ϵ for the V_σ state and the coarse-grained hybridization V between the V_σ and the π bath, in the untwisted bilayer graphene.

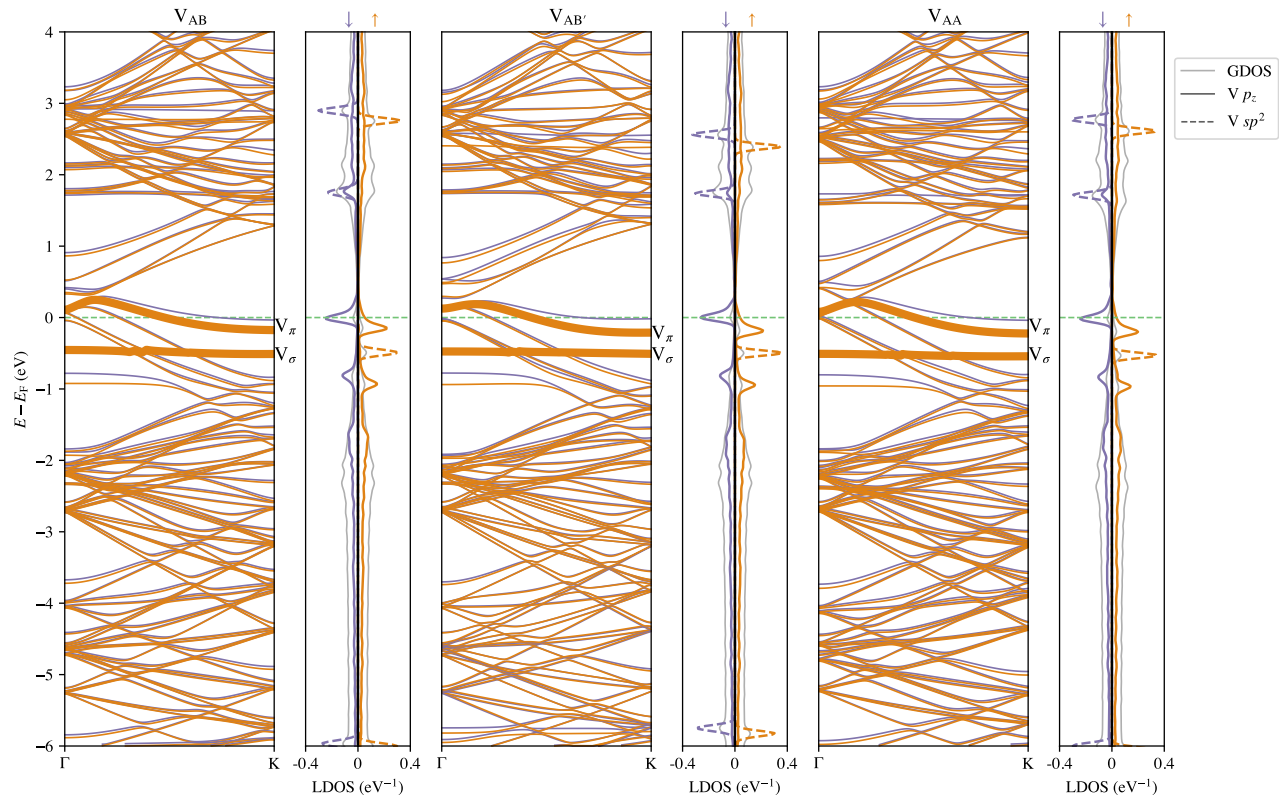


FIG. S3. The bands and local density of states (LDOS) as computed by the tight-binding model derived from Wannierized DFT results for the three vacancy configurations in untwisted bilayer graphene. The two vacancy states of interest, V_π and V_σ , are highlighted by the thick lines on the band structure plot.

three vacancy nearest-neighbor sites. The converged MLWFs at the three nearest neighbor sites are usually linear superpositions of each site's p_z and sp^2 orbitals. Therefore, we performed a unitary rotation within each 2×2 block such that the two onsite sp^2 and p_z orbitals have zero hopping. Then, we defined the orbital with lower chemical potential as the vacancy sp^2 orbital, and the higher one as the vacancy p_z orbital. Fig. S4 shows the MLWFs after this unitary rotation.

Figure S5 shows the wavefunctions of the two localized vacancy states in the spin-up channel, V_π and V_σ , at Γ . The V_σ state is mainly localized at the lone site among the three adjacent sites. In contrast, the V_π state (“zero mode”) is quasi-localized around the vacancy site, contributed by the dominant sublattice. In the following analysis, we will focus on the hybridization between the V_σ state and the π bath.

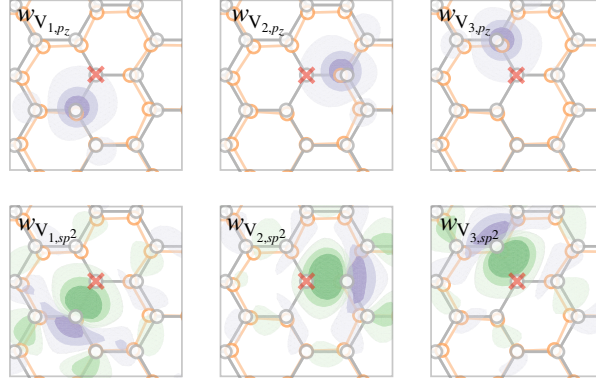


FIG. S4. The rotated maximally localized Wannier functions (MLWFs) at the three adjacent sites of the vacancy in the V_{AA} configuration. The red cross denotes the location of the vacancy site at the bottom layer.

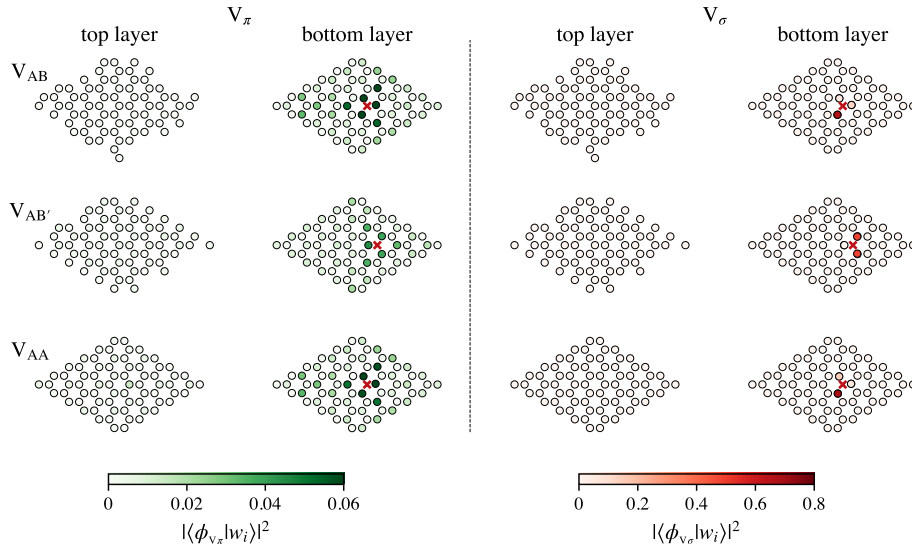


FIG. S5. The probability density projected onto the MLWFs orbitals for the two vacancy states of interest, V_σ and V_π , in V_{AA} configuration. Here, $|w_i\rangle$ is a $(N+2)$ vector, including $(N-1)$ π and 3 σ MLWFs. The dispersion of these two vacancy states is highlighted in Fig. S3. The V_π states are quasi-localized (power-law decay) around the vacancy site, while the V_σ states are exponentially localized at the vacancy adjacent sites.

B. Local corrugation enhances the V_σ -bath hybridization

We have also studied how local corrugation gives rise to non-zero hybridization between the V_σ states and the π bath in bilayer graphene. Figure S6(a) shows the atomic positions near the vacancy for the three equilibrium configurations. Compared to the other two cases, $V_{AB'}$ causes more local curvature on the top layer rather than the bottom layer where the vacancy resides. Figure S6(b) shows a distribution of the intra- and inter-layer sp^2 - p_z hoppings versus the distance away from the vacancy sp^2 orbitals. All the absolute values of the hoppings were collected and then averaged over a given bin at some distance. For V_{AA} and $V_{AB'}$ configurations, the nearest intra-layer hoppings are about 0.02 eV, and nearest inter-layer hoppings are halved, about 0.01 eV. For V_{AB} , the intra-layer hoppings are slightly larger, and the nearest inter-layer hoppings are 0.035 eV. This result is consistent with the estimated hybridization strength V for each configuration, as listed in Table SI, i.e., the hybridization between the V_σ and the π bath is mainly contributed by intralayer hoppings, which are caused by the local corrugation near the vacancy in the layer where the vacancy resides. The fact that the equilibrium structure is not completely flat allows the sp^2 and p_z orbitals to hybridize. Particularly, from the last two rows of the table, we see that the V_σ - π bath hybridization strength is further enhanced with the presence of the second layer that breaks the local mirror symmetry of the bilayer, in addition to the small local curvature induced by the vacancy. However, the finite hybridization strength

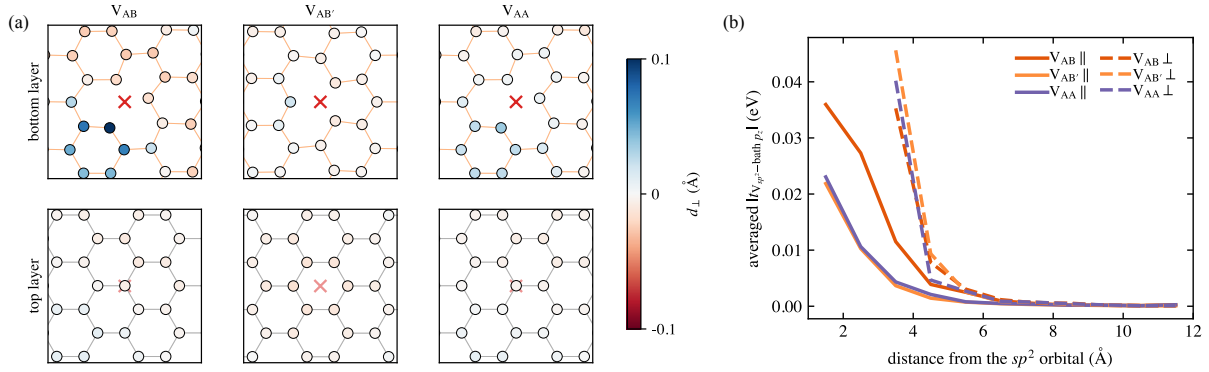


FIG. S6. After the relaxation of the lattice structure, local curvature forms near the regions of the vacancy. This local curvature gives rise to a non-zero intra-layer hopping (t_{\parallel}) between the vacancy sp^2 orbitals and the rest of the p_z orbitals. (a) Position of the atoms from the bottom and top layers of the three configurations, with the atoms colored by their z coordinate away from the averaged position. (b) The absolute values of the intra- (t_{\parallel}) and inter-layer hoppings (t_{\perp}) between the three vacancy sp^2 orbitals and the p_z orbitals, versus the distance away from the vacancy sp^2 orbitals. The values were averaged over the three vacancy-adjacent sites and coarse-grained with respect to the distance. We see that the intra-layer and inter-layer hoppings are of a similar order of magnitudes at equilibrium configurations.

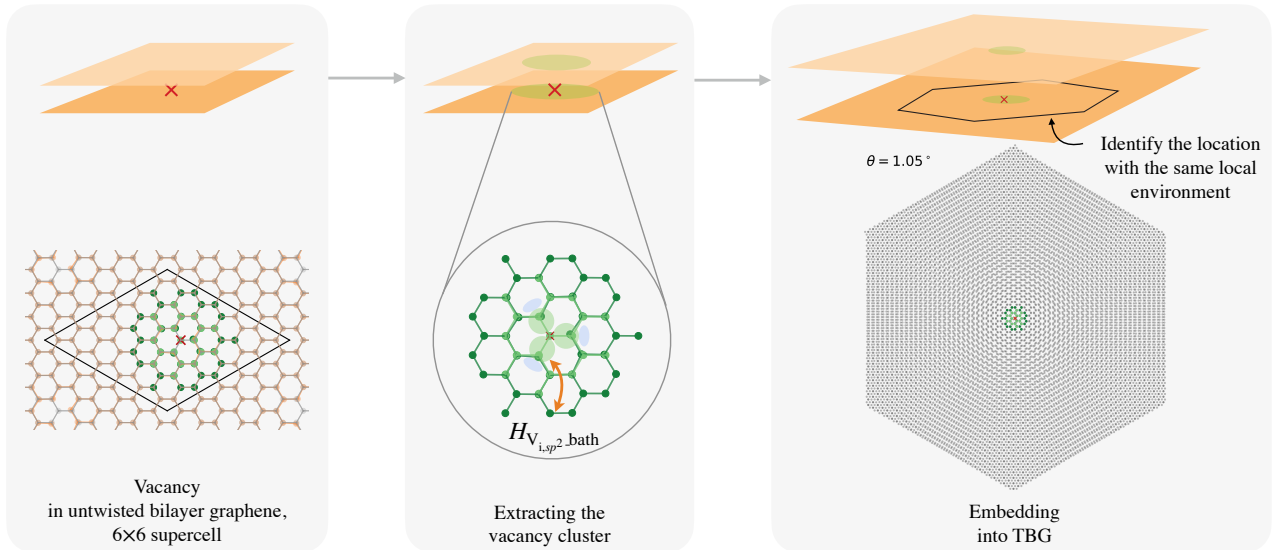


FIG. S7. A schematic of the workflow of modeling dilute impurities in moiré heterostructures, along with the example of applying it to modeling vacancies in TBG (in this work). 1. We start from simulating a certain type of impurity or vacancy in an untwisted bilayer structure (e.g., monovacancy in the AA-stacked bilayer graphene). The dark and light green sites represent the positions of the bath π orbitals from the bottom and top layers, respectively. 2. We then downfold to a model of all the p_z orbitals on all the sites, and the sp^2 orbitals on the three adjacent sites of the vacancy. We identify the cluster of atoms near the vacancy, both on the bottom layer and on the top layer, since they undergo significant in-plane lattice reconstruction and are mostly affected by the presence of the vacancy. 3. We then identify the corresponding location in a TBG that has the same local environment as in the bilayer graphene, either AA- or AB-stacked, and substitute all the hopping parameters near the vacancy with the ones obtained from the Wannierization.

gives a low Kondo temperature, which is not attainable in experiments. Therefore, similar to the situation in the single layer [S16], the local corrugation introduced by the substrate can help greatly increase the Kondo temperature. See Section ID for a detailed study of the effect of local corrugation near the vacancy.

Twist angle	1.05°			1.35°			2.0°		
	V_{AB}	$V_{AB'}$	V_{AA}	V_{AB}	$V_{AB'}$	V_{AA}	V_{AB}	$V_{AB'}$	V_{AA}
Hybridization strength V (eV)									
in [-200, 200] meV window	0.211(45)	0.135(21)	0.101(12)	0.192(65)	0.069(13)	0.092(12)	0.166(43)	0.075(9)	0.071(12)
in [-20, 20] meV window	0.152(16)	0.094(15)	0.106(2)	0.131(13)	0.062(4)	0.081(4)	0.157(6)	0.075(3)	0.070(2)

TABLE SII. Computed hybridization strength V between the V_σ and the π bath of TBG at various twist angles for the three vacancy configurations at equilibrium, within two chosen energy windows.

C. General framework of the multi-scale modeling of dilute impurities in moiré heterostructures

In our work, we have developed a general framework for modeling dilute impurities in moiré heterostructures. In the following section, we explain the details of this method with dilute vacancies in TBG as an example, which is the system of interest in our work. However, this method is readily generalizable for building the Anderson impurity model for impurities in any other moiré heterostructures. In TBG with commensurate twist angles, moiré unit cells usually include hundreds or thousands of atoms, making it computationally demanding for direct ab-initio simulations. Our method combines a much simpler ab-initio simulation of the impurity states on a smaller length scale and a description of the pristine moiré bath, circumventing the process of ab-initio downfolding the entire system from scratch.

Figure S7 shows the schematic workflow of this procedure. We start from a DFT calculation of a fully relaxed system of one vacancy in a 6×6 supercell of AA-stacked bilayer graphene (see supplementary section IA). We then Wannierize the bands near the Fermi level by downfolding to the p_z orbitals of the bath, and the sp^2 orbitals of the three adjacent vacancy sites. We then extract the hopping terms between the vacancy sp^2 orbitals, V_{i,sp^2} ($i = 1, 2, 3$) and the rest of the π orbitals at the $(N - 1)$ bath sites. We note that the hoppings among the sites that are close to the vacancy site (“vacancy cluster”) are mostly affected by the presence of the vacancy. The wavefunction $|\phi_{V\sigma}\rangle$ of the vacancy state of interest, V_σ , is obtained by diagonalizing the 3×3 block Hamiltonian of the V_{i,sp^2} basis. Then, we diagonalize the atomic-scale tight-binding model H_{TBG} for the pristine TBG as given by Ref. [S17] at twist angle θ and obtain the eigenstates $|\psi_{n\mathbf{k}}\rangle$, written in the π orbital basis.

In order to compute the hybridization function $\Delta(\omega)$, we will need to first compute the transition matrix elements $V_{n\mathbf{k}}$ between the vacancy states and mode $|\psi_{n\mathbf{k}}\rangle$.

Finally, we identify the location of the vacancy in TBG by searching for a local environment that is almost the same as that in the untwisted bilayer graphene. This method could be generalized to vacancies located in intermediate stacking regions. Here, this is easily achieved by identifying the AB or AA twist centers in TBG, then finding the atomic sites in TBG that have the closest local environment with each “bath” site in the untwisted bilayer graphene. We then replace all the original hoppings in the vacancy cluster in TBG with the ones we have derived from Wannierization, chosen to be within 6 Å away from the vacancy site at the bottom layer, and 4 Å away at the top layer. As a result, we constructed the hopping terms between V_{i,sp^2} and the π orbitals in TBG, i.e., $H_{V\sigma\text{-bath}}$. Therefore, by projecting the TBG eigenstates only onto the $(N - 1)$ bath π orbitals, the tunneling elements between $|\phi_{V\sigma}\rangle$ and the n th TBG eigenstates at \mathbf{k} is given by

$$V_{n\mathbf{k}} = \langle \phi_{V\sigma} | H_{V\sigma\text{-bath}} \mathcal{P}_{\text{bath-TBG}} | \psi_{n\mathbf{k}} \rangle. \quad (\text{S1})$$

The hybridization function between the V_σ state $|\phi_{V\sigma}\rangle$ and the TBG π bath is given by

$$\Delta_{\text{micro}}(\omega) = \pi \sum_{n,\mathbf{k}} |V_{n\mathbf{k}}|^2 \delta(\omega - E_{n\mathbf{k}}), \quad (\text{S2})$$

where the subscript “micro” denotes that this hybridization function is obtained from the atomic-scale, microscopic model of the TBG combined with ab-initio downfolded hopping terms obtained from DFT calculations.

We estimated the hybridization strengths V between the V_σ state and the π bath in TBG, within a chosen energy window around the Fermi level, using

$$\Delta_{\text{micro}}(\omega) \approx \pi V^2 \sum_{n,\mathbf{k}} |\langle \phi_{V\sigma} | \psi_{n\mathbf{k}} \rangle|^2 \delta(\omega - E_{n\mathbf{k}}), \quad (\text{S3})$$

which is equivalent to equation 3 in the main text. The averaged V is listed in Table IB, where the numbers in the brackets represent the standard deviations of the $V(\omega)$ within the chosen energy window. They are of similar values

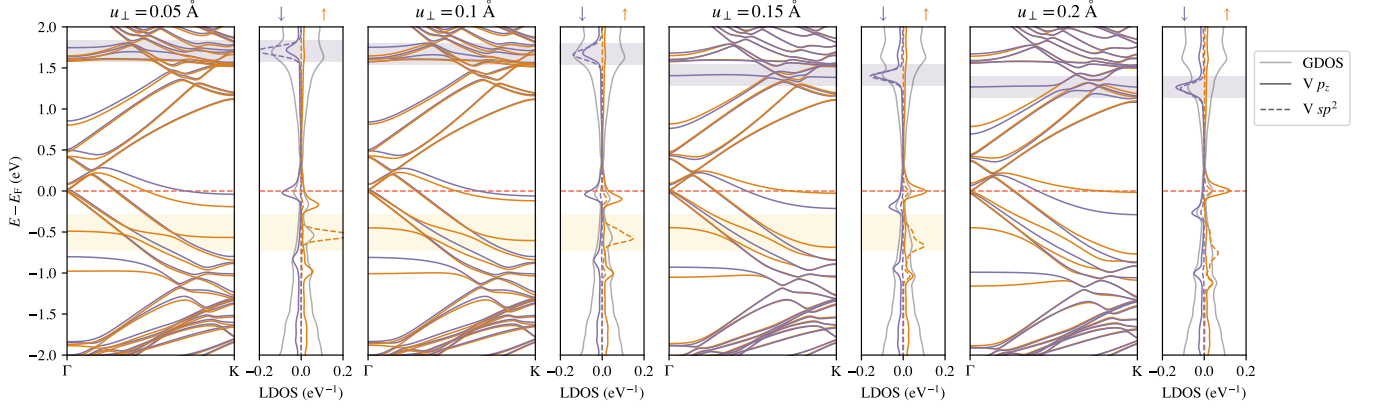


FIG. S8. The band structures of the untwisted bilayer graphene with V_{AA} type vacancy with local vertical displacements from 0.05 \AA to 0.2 \AA (see Fig. 1f for how the three vacancy-adjacent atoms are displaced). The highest occupied (lowest unoccupied) V_σ state is identified for $u_\perp < 0.2 \text{ \AA}$ and highlighted in yellow (purple). With $u_\perp = 0.2 \text{ \AA}$, a localized V_σ state is not identifiable due to the strong hybridization with the π bath.

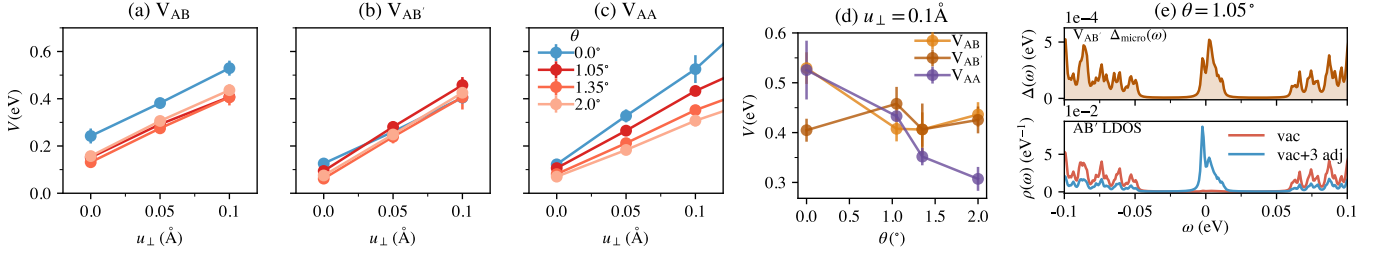


FIG. S9. (a-c) The computed hybridization strength for the three vacancy types, with ad-hoc local corrugations. (d) V versus the twist angle at $u_\perp = 0.1 \text{ \AA}$. The hybridization strength of V_{AA} vacancy is more sensitive to the twist compared to the other two AB-type vacancies. (e) The hybridization function for the $V_{AB'}$ in equilibrium configuration (upper panel) and the LDOS at the corresponding vacancy site, and the LDOS sum for the vacancy site and the three adjacent sites. We can see that the vacancy site of $V_{AB'}$ has almost zero contributions to the flat band DOS; when computing the value V , it would have a large uncertainty if one were to divide $\Delta(\omega)$ by the LDOS at only the vacancy site. Instead, we use the averaged LDOS of the vacancy and the three adjacent sites.

with the hybridization strengths in untwisted bilayer graphene. Curiously, we noticed that both V_{AB} and $V_{AB'}$'s V values show a larger standard deviation, compared with V_{AA} , especially as the twist angle approaches the magic angle 1.05° . We think this is because of the multifractal nature of the wavefunction in magic-angle TBG, which leads to very discontinuous flat-band wavefunctions in the atomic scale. Therefore, for these two cases, a simple frequency-independent V may not be sufficient to describe the hybridization function $\Delta(\omega)$. (Therefore, further NRG calculations with a more accurate $\Delta(\omega)$ need to be performed, which is beyond the scope of this study.)

Note that we used the same embedded cluster (see the green atoms in Fig. S7) for all these calculations. Therefore, the effect of the local curvature change in the vicinity of the vacancy due to different twist angles was not taken into account. We expect this approximation to apply to small twist angles where, for example, the V_{AA} vacancy only sees its local environment as AA. The AA and AB regions get small in TBG with large twist angles. Therefore, in this case, the local environment of a vacancy located at an AA (or AB) center can not be well approximated by AA- (or AB-) stacked untwisted bilayer graphene.

D. Local corrugation away from equilibrium

In a free-standing (no substrate) magic-angle TBG, the two layers naturally corrugate to lower its total energy, such that the interlayer distance in the AA regions is larger, and that in the AB regions is smaller. This natural corrugation is shown in Fig. 2(c) in the main text, where the positions of the C atoms in the TBG at $\theta = 1.05^\circ$ given by MD calculations are plotted, color-coded by their interlayer distances. However, we do not expect this natural corrugation introduced by twisting to enhance the hybridization significantly. This vertical corrugation is $\lesssim 0.1 \text{ \AA}$ [S18]

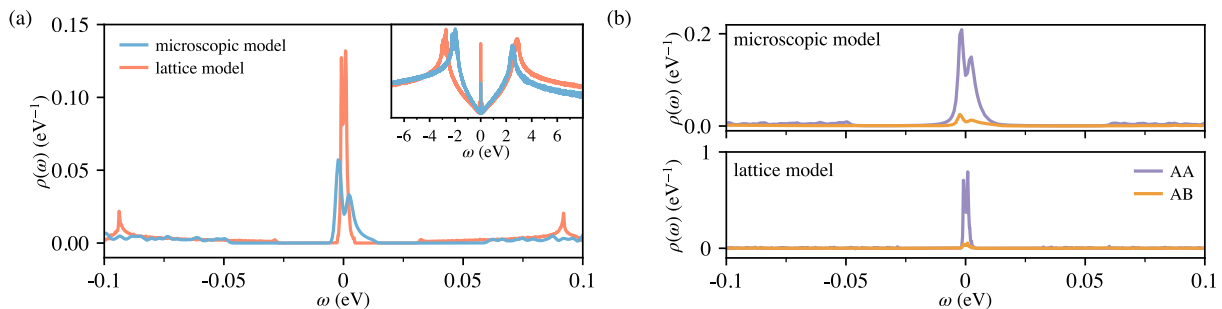


FIG. S10. A comparison of the GDOS and LDOS in AA and AB sites given by the two models: $\theta = 1.05^\circ$ microscopic model and $w = 0.11$ eV ($\alpha/\alpha_M = 1.0$) lattice model. Both these two models agree on the overall features of the GDOS (panel (a)) and LDOS (panel (b)). In NRG calculations, we chose to use the GDOS and LDOS produced by the lattice model to construct the hybridization function, which allows us to reach a larger system size and achieve higher resolution near the Fermi level.

in the moiré scale, and is therefore < 0.01 Å near the vacancy. In order to achieve an experimentally detectable Kondo temperature (> 1 K) for the vacancies in the AA regions, one needs to introduce local corrugations, especially near the vacancy, which greatly enhances the hybridization strength between the vacancy state V_σ and the bath. This could be achieved via coupling to a substrate that interacts slightly stronger with TBG compared with the widely used hBN [S16].

To systematically study the effect of local corrugation in enhancing the V_σ -bath hybridization V in untwisted bilayer graphene, and how this property gets preserved in TBG, we manually introduced vertical displacement for the three adjacent atoms near the vacancy and performed similar calculations as shown in section IC. We chose multiple vertical displacements u_\perp , then extracted V for the untwisted bilayer graphene, and TBG with chosen twist angles. Specifically, we moved the isolated, unbonded C atom upper by u_\perp and the other two bonded atoms lower by u_\perp . This fashion of introducing local corrugation is ad hoc, which is merely an attempt to mimic the substrate-induced local corrugation that was observed in experiments [S16] and to maximize the hybridization between the V_σ states and the π bath. To justify this, we performed two calculations: A. only displacing the isolated C atom by $+u_\perp$, and B. displacing the isolated C atom by $+u_\perp$ and the other two atoms by $-u_\perp$. For the V_{AA} vacancy with $u_\perp = 0.5$ Å, configuration A gives a hybridization strength $1.25(2)$ eV, smaller by $\sim 24\%$ than that given by configuration B. Therefore, we chose to displace the atoms using configuration B in order to maximize the hybridization strength.

The V values for V_{AA} were presented in Fig. 1(g). Here, we show the band structure plots for the chosen corrugations in Fig. S8. We see directly from the energies of the V_σ states in the spin up and down channels that the value of Hubbard U slightly decreases by ~ 0.1 eV as u_\perp increases to 0.1 Å (note the position of the lowest unoccupied spin-down V_σ state as highlighted in the light purple box), and the onsite energy ϵ almost does not change. However, the value of the total magnetic moment μ_{tot} decreases from $1.31 \mu_B$ to $1.17 \mu_B$ at $u_\perp = 0.1$ Å. In Fig. S9, we summarized the hybridization strengths for the three vacancy types as a function of the vertical displacement and the twist angle. Specifically, for $V_{AB'}$, the value of V is computed as $V = \sqrt{\Delta(\omega)/\bar{\rho}(\omega)}$, where $\bar{\rho}(\omega) = \frac{1}{4} \sum_{i \in \{\text{vac}, 3 \text{ adj-sites}\}} \rho_i(\omega)$, instead of just the LDOS at the vacancy site, which otherwise gives a huge uncertainty in V since the LDOS at the vacancy site almost vanishes near E_F (see Fig. S9(e)).

E. Comparison between the microscopic model and the lattice model

For NRG calculations, we used the parameters computed from our microscopic modeling of the TBG+vacancy system and the local density of states given by the lattice model (described in section II) to construct the hybridization function. The lattice model allows for finer resolution of the hybridization function near the Fermi level since a larger system size is more attainable. Figure S10 shows a direct comparison between the GDOS and the LDOS of the two models ($\theta = 1.05^\circ$ microscopic model and $w = 0.11$ eV lattice model). Both these two models agree on the overall features of the GDOS, i.e., they reproduce the flat band of a small bandwidth (20 meV for the microscopic model, 8 meV for the lattice model). As for the LDOS, both models reproduce the correct features in the AA and AB sites that the flat bands are more localized at the AA sites than the AB sites.

II. LATTICE MODEL OF TBG

The impurity host is a microscopic lattice model of TBG around the charge neutrality point where the angle enters as a free parameter [S19], which is derived from the Bistritzer–MacDonald continuum model [S20], and it has three main components

$$H_{\text{host}} = H_0 + H_{T_0} + H_{T_1}. \quad (\text{S4})$$

Here, H_0 denotes the lattice model of two independent Dirac cones, representing the two independent layers of graphene

$$H_0 = \sum_{\mathbf{r}, l} t \left[c_{\mathbf{r}, l}^\dagger \sigma_x c_{\mathbf{r}, l} + \sum_{j=1}^2 (c_{\mathbf{r}+\mathbf{a}_j, j}^\dagger \sigma^+ c_{\mathbf{r}, l} + \text{H.c.}) \right], \quad (\text{S5})$$

where $t = 2.8 \text{ eV}$, \mathbf{r} labels points on the triangular lattice, $c_{\mathbf{r}, l} = (c_{\mathbf{r}, \text{A}, l}, c_{\mathbf{r}, \text{B}, l})^T$ a pseudospinor operator, and layer $l = 1, 2$ with sublattices A, B. The tunneling between layers in real space is separated into two parts

$$\begin{aligned} H_{T_0} &= \sum_{\mathbf{r}} [c_{\mathbf{r}, 2}^\dagger \mathcal{T}_0(\mathbf{r}) c_{\mathbf{r}, 1} + \text{H.c.}], \\ H_{T_1} &= \sum_{\mathbf{r}} \sum_{n=1}^6 \left[(-1)^n c_{\mathbf{r}+\mathbf{a}_n, 2}^\dagger \mathcal{T}_1 \left(\mathbf{r} + \frac{\mathbf{a}_n}{2} \right) c_{\mathbf{r}, 1} + \text{H.c.} \right], \end{aligned} \quad (\text{S6})$$

where H_{T_0} denotes the interlayer tunneling at site \mathbf{r} , while H_{T_1} represents tunneling to the nearest neighbors on the triangular lattice of the other layer ($\mathbf{a}_n, n = 1, 2, \dots, 6$ are nearest-neighbor lattice vectors, $\mathbf{a}_1 = (\sqrt{3}/2, 3/2)d$, $\mathbf{a}_2 = (-\sqrt{3}/2, 3/2)d$, $\mathbf{a}_3 = (-\sqrt{3}, 0)d$, and $\mathbf{a}_j = -\mathbf{a}_{j-3}$ for $j = 4, 5, 6$. d is the nearest C atom distance. The lattice constant is $a_0 = |\mathbf{a}_j| = \sqrt{3}d$. The tunneling matrices are given by

$$\begin{aligned} \mathcal{T}_0(\mathbf{r}) &= \sum_{j=1}^3 \begin{pmatrix} w_0 \cos(\xi_{j,-}) & w_1 \cos(\zeta_{j,-}) \\ w_1 \cos(\zeta_{j,+}) & w_0 \cos(\xi_{j,+}) \end{pmatrix}, \\ \mathcal{T}_1(\mathbf{r}) &= \frac{1}{3\sqrt{3}} \sum_{j=1}^3 \begin{pmatrix} w_0 \sin(\xi_{j,-}) & w_1 \sin(\zeta_{j,-}) \\ w_1 \sin(\zeta_{j,+}) & w_0 \sin(\xi_{j,+}) \end{pmatrix}, \end{aligned} \quad (\text{S7})$$

where w_0, w_1 denotes the AA and AB tunneling, respectively. In the following, we define $w = w_1$ and fix the relation $w_0 = 0.75w$. The abbreviations are

$$\begin{aligned} \xi_{j,\pm} &= \mathbf{q}_j \cdot \mathbf{r} + \phi_j \pm \frac{1}{2}\theta, \\ \zeta_{j,\pm} &= \mathbf{q}_j \cdot \mathbf{r} \pm \frac{2}{3}\pi(j-1) + \phi_j, \end{aligned} \quad (\text{S8})$$

where θ is the twist angle contained in the twist wavevector $k_\theta = 2k_D \sin(\theta/2)$ with $k_D = 4\pi/(3\sqrt{3}d) = 4\pi/(3a_0)$. The three vectors are controlled by the k_θ as $q_1 = k_\theta(0, -1)$, $q_2 = k_\theta(\sqrt{3}/2, 1/2)$ and $q_3 = k_\theta(-\sqrt{3}/2, 1/2)$. ϕ_j are three global random phases. To ensure the boundary tunneling strengths are consistent, we need extra constraints in the system sizes L of the lattice, i.e., $\text{mod}(q_j(\theta)L_{x|y}, 2\pi) \approx 0$ for each θ . At the fixed angle $\theta = 1.05^\circ$, we choose $L \equiv L_x = L_y = 569a_0$. The boundary condition is taken to be a twisted boundary condition, i.e., a random twisted phase ψ on the hopping matrix elements at the (right) boundaries $t \rightarrow te^{i\psi}$.

Note that the particle-hole symmetry cannot be preserved in lattice models of TBG [S21] from the topology point of view. For each value of w , we shift the chemical potential (upon averaging twisted boundary conditions) to ensure charge neutrality.

III. KERNEL POLYNOMIAL METHOD

We computed the density of states using the kernel polynomial method (KPM). It is an approximation that expands a function using Chebyshev polynomials,

$$f(x) = \frac{1}{\pi\sqrt{1-x^2}} \left[g_0\mu_0 + 2 \sum_{n=1}^{\infty} g_n\mu_n T_n(x) \right], \quad (\text{S9})$$

where $T_n(x)$ s are the Chebyshev functions and $T_n(x) = \cos(n \arccos(x))$, $\mu_n = \int_{-1}^1 f(x) T_n(x)$ are the KPM expansion moments with Jackson kernel g_n [S22]. For the case of the global density of states (GDOS), the variable is E and we have,

$$\mu_n = \int_{-1}^1 \rho(E) T_n(E) = \frac{1}{D} \sum_{k=0}^{D-1} \langle k | T_n(H) | k \rangle = \frac{1}{D} \text{Tr}(T_n(H)), \quad (\text{S10})$$

where E is normalized to $[-1, 1]$, and the trace is evaluated stochastically with the number of random vectors N_R for the D states. The local density of states (LDOS) at site i is given by

$$\mu_n = \frac{1}{D} \langle i | T_n(H) | i \rangle. \quad (\text{S11})$$

To compute the density of states (DOS) with lattice size 569×569 , we used 2 random vectors ($N_R = 2$), and a number of expansions $N_C = 2^{18}$. The results were then averaged over a set of twisted boundary conditions, each of which was generated as a two-dimensional random phase vector and multiplied to the boundary Hamiltonian matrix entree.

The Wilson parameters for the NRG with certain logarithmic discretization Λ can be obtained from the GDOS/LDOS once the moments μ_n is computed [S23]. The key quantities are the integration of zeroth and the first moment of energies over logarithmic bins

$$\alpha_m^\pm = \pm \int_{\pm \tilde{\epsilon}_{m+1}}^{\pm \tilde{\epsilon}_m} \tilde{\Delta}(\tilde{\epsilon}) d\tilde{\epsilon}, \quad \beta_m^\pm = \pm \int_{\pm \tilde{\epsilon}_{m+1}}^{\pm \tilde{\epsilon}_m} \tilde{\epsilon} \tilde{\Delta}(\tilde{\epsilon}) d\tilde{\epsilon}, \quad (\text{S12})$$

where the tilde denotes the normalized energy and hybridization (GDOS/LDOS) and the logarithmic discretization $\tilde{\epsilon}_{m+1} < \pm \tilde{\epsilon} < \tilde{\epsilon}_m$, where

$$\tilde{\epsilon}_0 = 1, \quad \tilde{\epsilon}_m = \Lambda^{1-z-m} \quad \text{for } m = 1, 2, \dots \quad (\text{S13})$$

Using $T_n(x) = \cos(n \arccos x)$, and defining $\theta_m = \arccos \tilde{\epsilon}_m$ with $0 \leq \theta_m \leq \pi/2$ for $m = 0, 1, 2, \dots$, one can show that

$$\alpha_m^\pm = \frac{1}{\pi} \left[g_0 \mu_0 (\theta_{m+1} - \theta_m) + 2 \sum_{n=1}^{N_C-1} \frac{(\pm 1)^n}{n} g_n \mu_n (\sin n \theta_{m+1} - \sin n \theta_m) \right], \quad (\text{S14})$$

and

$$\begin{aligned} \beta_m^\pm = \frac{1}{\pi} \left[g_1 \mu_1 (\theta_{m+1} - \theta_m) + \sum_{n=1}^{N_C-2} \frac{(\pm 1)^n}{n} (g_{n-1} \mu_{n-1} + g_{n+1} \mu_{n+1}) (\sin n \theta_{m+1} - \sin n \theta_m) \right. \\ \left. + \sum_{n=N_C-1}^{N_C} \frac{(\pm 1)^n}{n} g_{n-1} \mu_{n-1} (\sin n \theta_{m+1} - \sin n \theta_m) \right]. \end{aligned} \quad (\text{S15})$$

Equations (S14) and (S15) are then inserted into the standard NRG unitary transformation to yield the Wilson-chain coefficients ε_n and t_n [S24].

A. Wavefunction from the lattice model of TBG

In TBG, as the twist angle is tuned across the magic angle, the wavefunction also changes to a critical multifractal state, which is neither expanded nor localized [S25, S26]. In Fig. S11(a) and (c), we show the wavefunction probability density $|\Psi(\mathbf{r})|^2$ (only at the bottom layer), in the real space and in the momentum space, for TBG described using the lattice model, with $\alpha/\alpha_M = 0.27, 0.82, 1.0$. When the system is away from the magic angle (top panel, 0.27), the wavefunction is very delocalized and, therefore, shows a large peak at the moiré \bar{K} point. As the system approaches the magic angle ($\alpha/\alpha_M = 1.0$), the wavefunction becomes more localized and shows more satellite peaks around the original peak at \bar{K} .

The multifractal nature of the wavefunction is characterized by the q th moment of the wavefunction probability density in either the real space or the momentum space.

$$\mathcal{I}_R(q) = L^d \sum_{\mathbf{r}} |\Psi(\mathbf{r})|^{2q}, \quad \mathcal{I}_M(q) = \sum_{\mathbf{k}} |\Psi(\mathbf{k})|^{2q}, \quad (\text{S16})$$

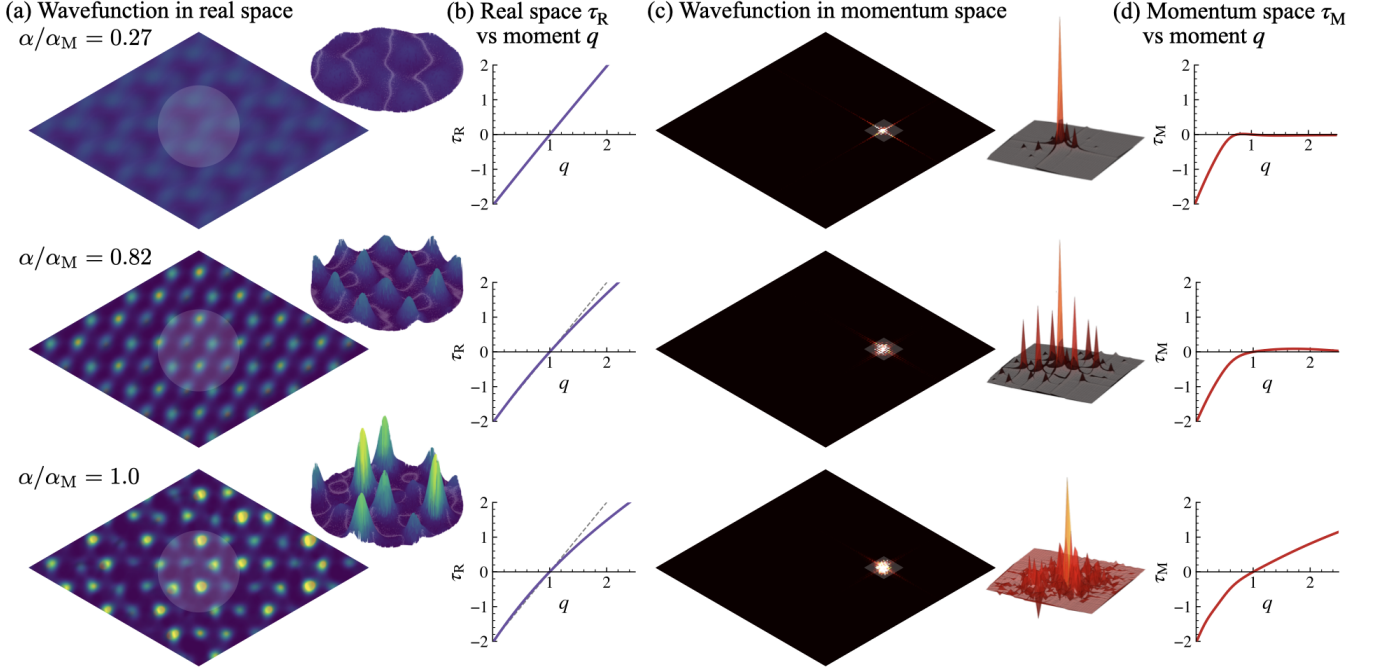


FIG. S11. Multifractal nature of the TBG wavefunction at the magic angle. (a) The wavefunctions in real space for α/α_M at 0.27, 0.82, and 1.0, along with the zoom-in to a few moiré cells. (b) The scaling exponent τ_R versus moment q , computed using the real-space q th moment of the wavefunction with binning sizes $B_1 = 8$, $B_2 = 16$. The dashed lines represent $\tau_R = 2(q - 1)$ (the plane wave limit). (c) The Fourier transform of the wavefunctions to the momentum space, along with the zoom-in to the moiré Brillouin zone. (d) The scaling exponent τ_M versus moment q , computed using the momentum-space q th moment of the wavefunction with binning sizes $B_1 = 4$, $B_2 = 6$.

where $\Psi(\mathbf{k}) = \frac{1}{\sqrt{N}} \sum_{\mathbf{r}} e^{i\mathbf{k}\cdot\mathbf{r}} \Psi(\mathbf{r})$, and \mathbf{k} is the \mathbf{k} grid commensurate with the real-space lattice sites (no periodic boundary conditions are assumed for the incommensurate lattice model, though). Here, L is the system's linear scale, and d is the spatial dimension (2 in the case of TBG). When $q = 2$, this definition is consistent with the common definition of the inverse participation ratio.

For a plane wave state, with the normalization of the wavefunction taken into account, one can see that $\mathcal{I}_R(q) \sim L^d \times L^{qd} = L^{d(1+q)}$. Let us define the scaling exponent τ_R as $\mathcal{I}_R(q) \sim L^{-\tau_R}$, we can see that for a plane wave state, $\tau_R(q) = d(q - 1)$ [S25]. In contrast to the constant d value, the critical multifractal state is characterized by that $\tau_R(q) = d_q(q - 1)$, where d_q depends on the power q of the moments.

Figure S11(b) and (d) show the scaling exponents computed using real-space wavefunction and momentum-space wavefunction, τ_R and τ_M , as a function of q . For $\alpha/\alpha_M = 1.0$, τ_R deviates from the linear relationship of a plane-wave-like wavefunction, and τ_M also shows a strong dependence on q . For the other two cases away from the magic angle, τ_R is closer to the plane wave $2(q - 1)$ line (denoted by the dashed lines in panel (b)), and τ_M freezes for $q > 2$, showing the ballistic character of the wavefunction in momentum space (i.e., the wavefunction is quite spread out in real space). The $\tau_{R/M}$ values were calculated using the method described below (see also the supplemental note 5 of Ref. [S26]).

To compute the scaling exponent $\tau_{R/M}$, we introduce a binning factor B and recompute the wavefunction averaged in the real-space bins (or on a coarse \mathbf{k} grid). To extract τ , the following approximation is used for two consecutive binning factors B_1 and B_2 , which yields similar results with fitting $\ln \mathcal{I}_{R/M}(q, B)$ vs $\ln B$ to a line,

$$\tau_{R/M}(q; B_1, B_2) = \frac{\ln \mathcal{I}_{R/M}(q, B_1) - \ln \mathcal{I}_{R/M}(q, B_2)}{\ln B_1 - \ln B_2}. \quad (\text{S17})$$

The implications of the multifractal nature of TBG wavefunctions are profound, and the physics can only be accessible through the incommensurate lattice model, but not the commensurate tight-binding model. It has been shown in several disordered models [S25, S27–S33], and some quasiperiodic settings [S23, S34], at Anderson localization transitions, the multifractal wavefunctions lead to physical observables acquiring broad distributions. This arises because multifractal wavefunctions have probability amplitudes that are spatially distributed in a highly non-trivial fashion. In our work, the exact distribution of the Kondo temperatures is obtained using NRG, and also shows a long

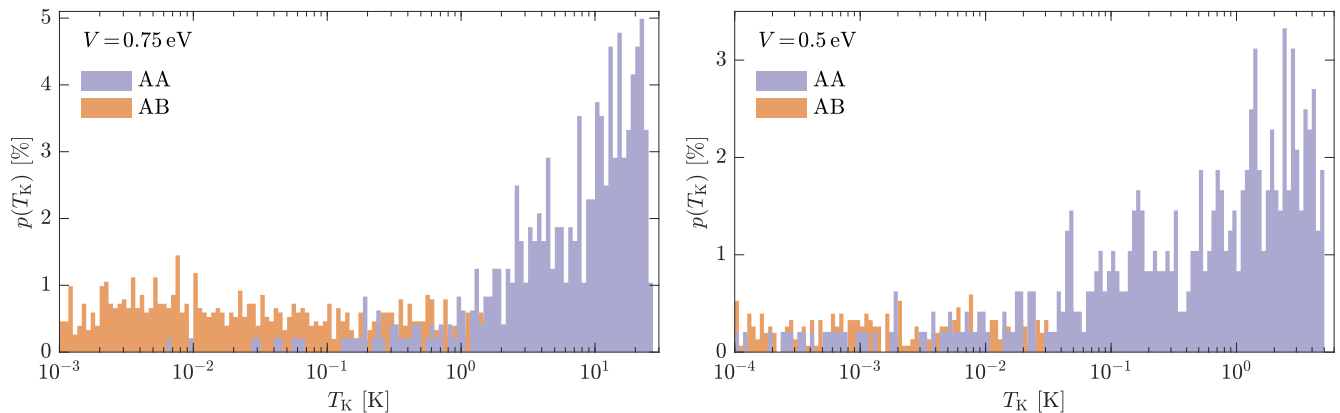


FIG. S12. Distribution of T_K for different impurity locations across magic-angle TBG, analogously to Fig. 4 in the main text, but at smaller hybridization strengths $V=0.75$ eV and $V=0.5$ eV.

tail into the lower temperatures. Using our method, we have access to all the possible locations in either the AA or the AB regions of TBG that highly mimic the realistic scenario, it is potentially possible to verify our predictions using STM experiments combined with vacancies created by in-situ Helium sputtering on TBG [S35].

IV. NUMERICAL RENORMALIZATION GROUP

We used an NRG discretization parameter of $\Lambda = 3$ and kept up to 2000 SU(2) multiplets during the iterative diagonalization. The impurity contribution to the spin susceptibility was computed as a thermodynamic property (we average over several values of β on the order of 1, cf. Eq. (45) in Ref. [S24]). The local spin susceptibility was computed within the full density-matrix NRG [S36, S37]. To demonstrate how sensitive T_K is to V , we plot in Fig. S12 the distribution of Kondo temperatures, analogously to Fig. 4 in the main text, but at two lower values of V .

Figure S13 shows the GDOS for various twist angles from $\alpha=0$ to α_M on linear and logarithmic scales, together with the corresponding hopping amplitudes along the Wilson chain t_n . All lines are shifted vertically for visualization. Consider $\alpha < \alpha_M$ first. From the log-log plot of the GDOS, one sees that all curves behave as $\rho(\omega) \propto |\omega|$ for low frequencies, but the KPM resolution is low below $|\omega| \lesssim 10^{-2}$ eV and breaks down for $|\omega| \lesssim 10^{-3}$ eV. Accordingly, the Wilson chain hopping parameters t_n become irregular for $n \gtrsim 15$ and spuriously flat for $n \gtrsim 20$ (as the GDOS levels off below the resolution limit). For α closer α_M , more low-energy states are available to KPM and the low-energy resolution becomes better. At α_M , ρ is actually flat at low energy and the t_n actually follow the asymptotic $\Lambda^{-n/2}$ behavior, so the resolution limit is not seen. To overcome the KPM resolution limit for $\alpha < \alpha_M$ and access arbitrarily small energy scales (for all α), we adjust and extend the Wilson chain parameters using the analytically known asymptotic behavior as in Eqs. (28) and (29) of Ref. [S38] for $\alpha < \alpha_M$ and Eq. (32) of Ref. [S24] for $\alpha = \alpha_M$. Note that this is equivalent to extrapolating the hybridization function to very low energies.

-
- [S1] G. Kresse and J. Hafner, *Ab initio* molecular dynamics for liquid metals, *Phys. Rev. B* **47**, 558 (1993).
 - [S2] G. Kresse and J. Furthmüller, Efficiency of ab-initio total energy calculations for metals and semiconductors using a plane-wave basis set, *Comput. Mater. Sci.* **6**, 15 (1996).
 - [S3] G. Kresse and J. Furthüller, Efficient iterative schemes for *ab initio* total-energy calculations using a plane-wave basis set, *Phys. Rev. B* **54**, 11169 (1996).
 - [S4] J. P. Perdew, K. Burke, and M. Ernzerhof, Generalized Gradient Approximation Made Simple, *Phys. Rev. Lett.* **77**, 3865 (1996).
 - [S5] P. A. Thrower and R. M. Mayer, Point defects and self-diffusion in graphite, *Physica Status Solidi (a)* **47**, 11 (1978).
 - [S6] B. R. K. Nanda, M. Sherafati, Z. S. Popović, and S. Satpathy, Electronic structure of the substitutional vacancy in graphene: density-functional and Green's function studies, *New J. Phys.* **14**, 083004 (2012).
 - [S7] J. J. Palacios and F. Ynduráin, Critical analysis of vacancy-induced magnetism in monolayer and bilayer graphene, *Phys. Rev. B* **85**, 245443 (2012).
 - [S8] M. Leccese and R. Martinazzo, Anomalous delocalization of resonant states in graphene & the vacancy magnetic moment, *Electron. Struct.* **5**, 024010 (2023).

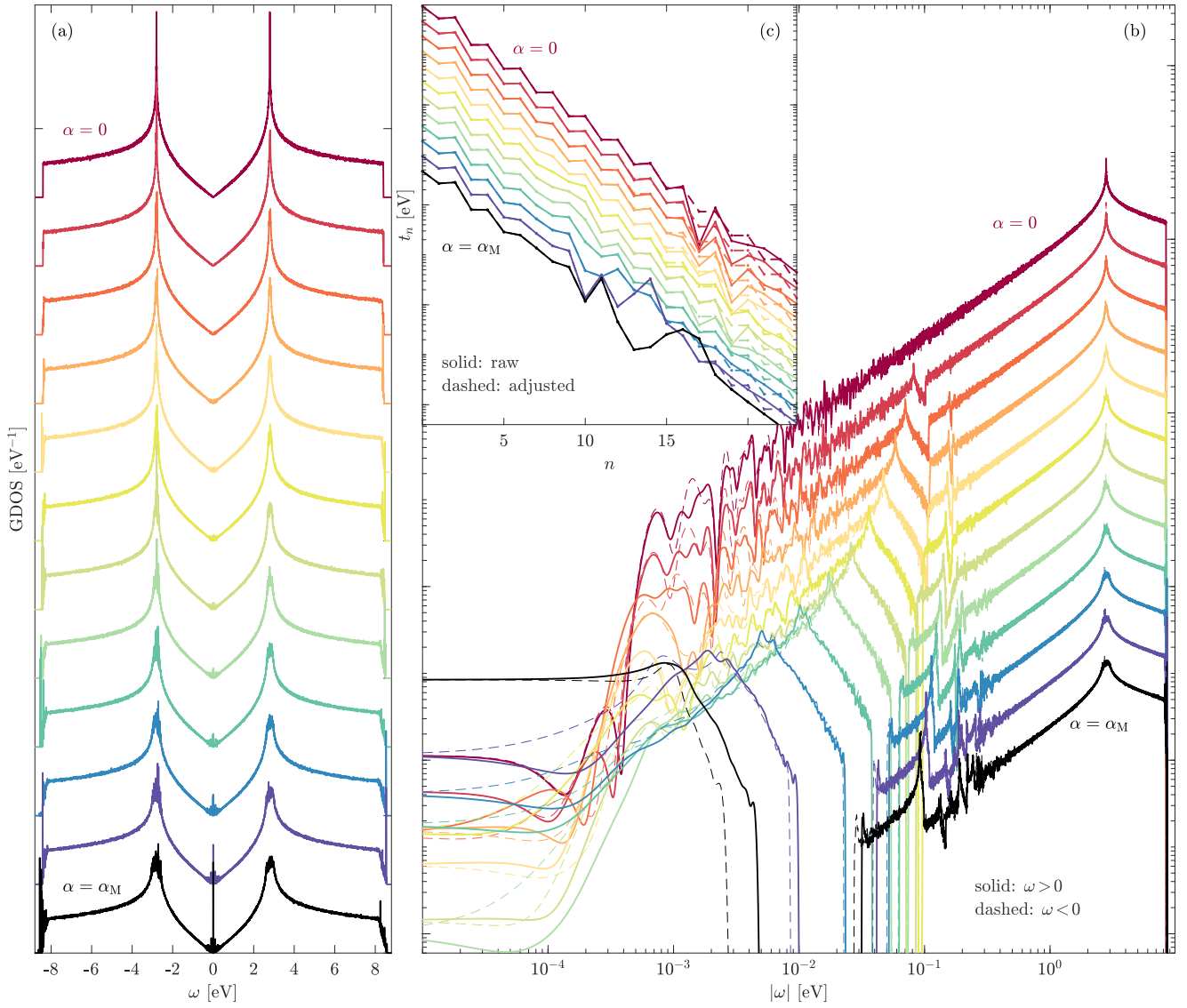


FIG. S13. GDOS for various twist angles on (a) linear and (b) logarithmic scales. (c) Corresponding hopping amplitudes along the Wilson chain. All lines are shifted vertically for visualization.

- [S9] V. G. Miranda, L. G. G. V. Dias Da Silva, and C. H. Lewenkopf, Coulomb charging energy of vacancy-induced states in graphene, *Phys. Rev. B* **94**, 075114 (2016).
- [S10] M. Schüler, M. Rösner, T. O. Wehling, A. I. Lichtenstein, and M. I. Katsnelson, Optimal Hubbard Models for Materials with Nonlocal Coulomb Interactions: Graphene, Silicene, and Benzene, *Phys. Rev. Lett.* **111**, 036601 (2013).
- [S11] H. J. Changlani, H. Zheng, and L. K. Wagner, Density-matrix based determination of low-energy model Hamiltonians from ab initio wavefunctions, *J. Chem. Phys.* **143**, 102814 (2015).
- [S12] N. Marzari and D. Vanderbilt, Maximally localized generalized Wannier functions for composite energy bands, *Phys. Rev. B* **56**, 12847 (1997).
- [S13] A. A. Mostofi, J. R. Yates, Y.-S. Lee, I. Souza, D. Vanderbilt, and N. Marzari, wannier90: A tool for obtaining maximally-localised Wannier functions, *Comput. Phys. Commun.* **178**, 685 (2008).
- [S14] A. A. Mostofi, J. R. Yates, G. Pizzi, Y.-S. Lee, I. Souza, D. Vanderbilt, and N. Marzari, An updated version of wannier90: A tool for obtaining maximally-localised Wannier functions, *Comput. Phys. Commun.* **185**, 2309 (2014).
- [S15] G. Pizzi, V. Vitale, R. Arita, S. Blügel, F. Freimuth, G. Géranton, M. Gibertini, D. Gresch, C. Johnson, T. Koretsune, J. Ibañez-Azpiroz, H. Lee, J.-M. Lihm, D. Marchand, A. Marrazzo, Y. Mokrousov, J. I. Mustafa, Y. Nohara, Y. Nomura, L. Paulatto, S. Poncé, T. Ponweiser, J. Qiao, F. Thöle, S. S. Tsirkin, M. Wierzbowska, N. Marzari, D. Vanderbilt, I. Souza, A. A. Mostofi, and J. R. Yates, Wannier90 as a community code: new features and applications, *J. Phys.: Condens. Matter* **32**, 165902 (2020).
- [S16] Y. Jiang, P.-W. Lo, D. May, G. Li, G.-Y. Guo, F. B. Anders, T. Taniguchi, K. Watanabe, J. Mao, and E. Y. Andrei,

- Inducing Kondo screening of vacancy magnetic moments in graphene with gating and local curvature, *Nat. Commun.* **9**, 2349 (2018).
- [S17] S. Pathak, T. Rakib, R. Hou, A. Nevidomskyy, E. Ertekin, H. T. Johnson, and L. K. Wagner, Accurate tight-binding model for twisted bilayer graphene describes topological flat bands without geometric relaxation, *Phys. Rev. B* **105**, 115141 (2022).
- [S18] K. Krongchon, T. Rakib, S. Pathak, E. Ertekin, H. T. Johnson, and L. K. Wagner, Registry-dependent potential energy and lattice corrugation of twisted bilayer graphene from quantum Monte Carlo, *Phys. Rev. B* **108**, 235403 (2023).
- [S19] J. H. Wilson, Y. Fu, S. Das Sarma, and J. H. Pixley, Disorder in twisted bilayer graphene, *Phys. Rev. Res.* **2**, 023325 (2020).
- [S20] R. Bistritzer and A. H. MacDonald, Moiré bands in twisted double-layer graphene, *Proc. Natl. Acad. Sci. U.S.A.* **108**, 12233 (2011).
- [S21] Z.-D. Song, B. Lian, N. Regnault, and B. A. Bernevig, Twisted bilayer graphene. II. Stable symmetry anomaly, *Phys. Rev. B* **103**, 205412 (2021).
- [S22] A. Weiße, G. Wellein, A. Alvermann, and H. Fehske, The kernel polynomial method, *Rev. Mod. Phys.* **78**, 275 (2006).
- [S23] A.-K. Wu, D. Bauernfeind, X. Cao, S. Gopalakrishnan, K. Ingersent, and J. H. Pixley, Aubry-André Anderson model: Magnetic impurities coupled to a fractal spectrum, *Phys. Rev. B* **106**, 165123 (2022).
- [S24] R. Bulla, T. A. Costi, and T. Pruschke, Numerical renormalization group method for quantum impurity systems, *Rev. Mod. Phys.* **80**, 395 (2008).
- [S25] S. Kettemann, E. R. Mucciolo, I. Varga, and K. Slevin, Kondo-Anderson transitions, *Phys. Rev. B* **85**, 115112 (2012).
- [S26] Y. Fu, E. J. König, J. H. Wilson, Y.-Z. Chou, and J. H. Pixley, Magic-angle semimetals, *npj Quantum Mater.* **5**, 71 (2020).
- [S27] V. Dobrosavljević, T. R. Kirkpatrick, and B. G. Kotliar, Kondo effect in disordered systems, *Phys. Rev. Lett.* **69**, 1113 (1992).
- [S28] E. Miranda, V. Dobrosavljević, and G. Kotliar, Kondo disorder: a possible route towards non-Fermi-liquid behaviour, *J. Phys.: Condens. Matter* **8**, 9871 (1996).
- [S29] P. S. Cornaglia, D. R. Grempel, and C. A. Balseiro, Universal Distribution of Kondo Temperatures in Dirty Metals, *Phys. Rev. Lett.* **96**, 117209 (2006).
- [S30] S. Kettemann, E. R. Mucciolo, and I. Varga, Critical Metal Phase at the Anderson Metal-Insulator Transition with Kondo Impurities, *Phys. Rev. Lett.* **103**, 126401 (2009).
- [S31] V. G. Miranda, L. G. G. V. Dias da Silva, and C. H. Lewenkopf, Disorder-mediated Kondo effect in graphene, *Phys. Rev. B* **90**, 201101 (2014).
- [S32] R. Gammag and K.-S. Kim, Distribution of critical temperature at Anderson localization, *Phys. Rev. B* **93**, 205128 (2016).
- [S33] K. Slevin, S. Kettemann, and T. Ohtsuki, Multifractality and the distribution of the Kondo temperature at the Anderson transition, *EPJ B* **92**, 281 (2019), arXiv:1910.00917 [cond-mat].
- [S34] E. C. Andrade, A. Jagannathan, E. Miranda, M. Vojta, and V. Dobrosavljević, Non-fermi-liquid behavior in metallic quasicrystals with local magnetic moments, *Phys. Rev. Lett.* **115**, 036403 (2015).
- [S35] A. M. Coe, G. Li, and E. Y. Andrei, (2024), arXiv:2404.05002 [cond-mat.mes-hall].
- [S36] R. Peters, T. Pruschke, and F. B. Anders, Numerical renormalization group approach to green's functions for quantum impurity models, *Phys. Rev. B* **74**, 245114 (2006).
- [S37] A. Weichselbaum and J. von Delft, Sum-rule conserving spectral functions from the numerical renormalization group, *Phys. Rev. Lett.* **99**, 076402 (2007).
- [S38] R. Bulla, T. Pruschke, and A. C. Hewson, Anderson impurity in pseudo-gap Fermi systems, *J. Phys.: Condens. Matter* **9**, 10463 (1997).